Effective viscosity of 2D suspensions - Confinement effects

Vincent Doyeux, Stephane Priem, Levan Jibuti, Alexander Farutin, Mourad Ismail, Philippe Peyla

Effective viscosity of 2D suspensions - Confinement effects.

Vincent Doyeux,[1,2] Stephane Priem,[1,2] Levan Jibuti,[3]
Alexander Farutin,[1,2] Mourad Ismaïl,[1,2] and Philippe Peyla[1,2,*]

[1] *University Grenoble Alpes, LIPhy, F-38000 Grenoble, France*
[2] *CNRS, LIPhy, F-38000 Grenoble, France*
[3] *Theoretische Physik I, University of Bayreuth, 95440 Bayreuth, Germany*

(Dated: Received: March 17, 2016/ Revised version: (date))

We study the rheology of a sheared $2D$ suspension of non-Brownian disks in presence of walls. Although, it is of course possible today with modern computers and powerful algorithms to perform direct numerical simulations that fully account for multiparticle $3D$ interactions in the presence of walls, the analysis of the simple case of a $2D$ suspension, provides valuable insights and helps to understand $3D$ results. Thanks to the direct visualization of the whole $2D$ flow (the shear plane), we are able to give a clear interpretation of the full hydrodynamics of semi-dilute confined suspensions. For instance, we examine the role of particle-wall and particle-particle interactions to determine the effective viscosity of confined sheared suspensions. We provide numerical estimates of the intrinsic viscosity $[\eta]$ as well as of the contribution of hydrodynamic interactions β to the effective viscosity for a wide range of confinements. As a benchmark for our simulations, we compare the numerical results obtained for $[\eta]$ and β for very weak confinements with analytical values $[\eta]_\infty$ and β_∞ obtained for an infinite fluid. If the value $[\eta]_\infty = 2$ is well known in the literature, much less is published on β value. Here, we analytically calculate with a very high precision $\beta_\infty = 3.6$. Finally, we re-examine the $3D$ case in the light of our $2D$ results.

* philippe.peyla@univ-grenoble-alpes.fr

I. INTRODUCTION

Understanding the macroscopic transport and flow behavior of particles or fibers suspended in a fluid medium is important to several industries that handle slurries, ceramics, colloids, or polymers for example. Usually negligible or small Reynolds numbers (Re) are considered since this situation is more relevant regarding the high viscosity of suspensions. An external flow makes move micron-scale objects that are strongly coupled to each other by hydrodynamic interactions (HI) [1–3]. $2D$ simulations represent an efficient and convenient tool for understanding some phenomena arising in hydrodynamics of suspensions. For example, $2D$ simulations have been currently used to study flow past $2D$ single bodies of arbitrary cross-sectional shape [4] or around rotating circular cylinder in a shear flow at low Reynolds number [5]. $2D$ simulations have also been used to study multiparticle systems such as diffusing proteins in biological membranes [6], suspensions of red blood cells [7], vesicles [8] or capsules [9, 10]. $2D$ simulations are much less time and memory consuming than $3D$ ones. In $2D$, very simple visualizations of the entire flow are easy and render a clear insight of $3D$ problems that are sometimes quite difficult to understand. Several publications have been dedicated to $2D$ suspensions and their rheology from dilute to large volume fractions [11, 12]. In this paper, we are interested in the rheology of confined suspensions.

Low Re number flows of suspensions of neutrally buoyant particles sheared or confined between two walls [13–21] or transported through channels [7, 22–25] of width comparable to the particle dimension are very important because of their occurrence in many experimental, biological, and technological systems including blood flow in capillaries or in confined flows [7], but also flows in porous media [26] or in microfluidic devices [27].

It was shown [19] that the contribution of $3D$ hydrodynamics interactions in the semi-dilute regime to the effective viscosity becomes negative for very confined hard and non-Brownian spheres. This effect was further confirmed by another theoretical approach [21] and by experiments [20]. This effect survives for finite Re numbers ($Re \approx 5$) [28]. In this work, we observe the same phenomenon for the $2D$ case (with $Re = 0$) and we can give a simple interpretation of the variation of the effective viscosity with confinement by examining the dissipation density and the fluid flow around particles. Our $2D$ simulations can clarify points that were still unclear such as the contribution of the HI to the effective viscosity in high confinement cases. We focus our study on particle-wall HI in the dilute case and particle-particle HI in presence of walls for semi-dilute $2D$ suspensions.

The volume fraction ϕ is usually defined as the total volume of N spherical particles of radius a divided by the whole volume V of the suspension: $\phi_{3D} = N\frac{4}{3}\pi a^3/V$. Here in $2D$, we define a surface fraction $\phi_{2D} = N\pi a^2/S$ where S represents the total surface of the suspension. For convenience, in the rest of the paper, we drop the $2D$ subscript and we refer to the volume fraction even in $2D$. When we refer to the $3D$ case, no ambiguity remains. Whatever the dimension, the effective viscosity of the whole suspension depends non-linearly on ϕ and can be expressed as a virial expansion [3] in the semi-dilute case where pair interactions start to operate between particles:

$$\eta_{eff} = \eta_0 \left[1 + [\eta]\phi + \beta\phi^2 + O(\phi^3)\right], \tag{1}$$

where $[\eta]$ is the intrinsic viscosity, representing the contribution of each particle to η_{eff}. The coefficient β is the contribution of HI between pairs of particles to η_{eff}. Previous studies [11, 12] on rheology of $2D$ suspensions have generally focused on the behavior of η_{eff} on a large domain of volume fraction and fit $\eta_{eff}(\phi)$ with the empirical law of Krieger and Dougherty [29]. In this paper, we would like to understand the effect of HI between pairs of confined particles on the effective viscosity, we thus restrain ourselves to semi-dilute regimes where the virial expansion of η_{eff} [eq.(1)] is valid to order ϕ^2.

For an infinite $3D$ fluid, the values of $[\eta]_\infty$ and β_∞ are very well known. Since Einstein's seminal calculations which determined $[\eta]_\infty = 2.5$ [30, 31], the contribution of HI to η_{eff} for non-Brownian suspensions of uniformely distributed hard spheres has been calculated by Batchelor and Green [32] who found $\beta_\infty = 5.2 \pm 0.3$, then further accurate calculations gave a value of β_∞ very close to 5.0 [33, 34]. In $2D$, if the intrinsic viscosity $[\eta]_\infty = 2$ is a well known value [35, 36], the $2D$ β_∞ value is less reported in the literature where $\beta_\infty = 4.0$ was calculated for the shear modulus of a $2D$ incompressible solid suspension of uniformely distributed disks [37]. Here, we show that the value is in fact closer to $\beta_\infty = 3.6$ with a very accurate analytical calculation (see Appendices A,B and C).

In order to properly investigate the rheology, the suspension is submitted to a shear rate between two moving walls where no-slip boundary conditions are used. The effective viscosity is calculated by integrating the dissipation in the liquid phase. Details of the numerical $2D$ method based on finite elements are given below. In view of benchmarking our simulations, we compare $[\eta]$ and β obtained for vanishing confinements to analytical results $[\eta_\infty]$ and β_∞. In the dilute case, *i.e.* for $[\eta]$, we perfomed very accurate analytical calculations which gives the value of $[\eta]$ in presence of a single wall. In the semi-dilute case, *i.e.* regarding β, we numerically analyze the particle-particle HI within a uniform distribution of non-Brownian disks with a very weak confinement, we find $\beta = 3.6 \pm 0.1$ very close to the analytically value $\beta_\infty = 3.6$.

We find that the main source of dissipation arises in the fluid region between particles and walls. But another important source of dissipation lies in the region between two particles that are at $45°$ (mod $90°$) from each other

(the 0°-angle is taken from horizontal position when particles are aligned along the flow parallel to the walls). While increasing confinement, local dissipation density increases between each particle and walls but decreases between particles because of the disappearance of 45° configurations due to the geometrical constraint. The increasing of dissipation between particles and walls is a contribution of each individual particle (*i.e.* it is a linear ϕ-variation) and it increases $[\eta]$. If the latter effect can be expected, we also observe a much less predictable phenomenon: the creation of "dips" of dissipation between aligned and close particles, where locally, dissipation is less than the dissipation created by the shear flow without particles. Thus, an aligned pair of particles along the flow dissipates less than two non-interacting particles: this is the contribution of pairs of particles to dissipation (*i.e.* a ϕ^2-variation) and it leads to a negative contribution to the HI and explains the negativeness of β. This phenomenon finds its origin in the slow-down of the angular velocity of each particle due to their mutual interaction within the pair aligned along the flow. In light of this $2D$ interpretation, we checked that this result holds in $3D$.

The paper is organized as follows, in section 2 we present the numerical method, in section 3 we show the results concerning particle-wall and particle-particle HI. Then, we compare our results with the $3D$ case. For sake of readability, details of analytical calculations are given in appendixes A, B, C and D. Then in section 4, we conclude.

II. NUMERICAL MODEL

From the modeling point of view, our problem can be seen as a fluid/structure interaction. Therefore, it could be modeled by a coupling between Stokes equations for the dynamics of the surrounding incompressible fluid and Newton-Euler equations for the motion of rigid bodies. The action of the fluid on the particles is modeled by the hydrodynamic forces and torques acting on particles' surface and they can be considered as the right hand side of Newton-Euler equations. In addition, particles interact with the surrounding fluid using a no-slip boundary condition in Stokes equations. However, this explicit coupling can be unstable numerically and its resolution often requires very small time step. In addition, as we have chosen to use Finite Elements Method FEM (for accuracy reasons) and since the positions of particles change with time, we have to remesh the computational domain at each time step or in best cases at every few time steps.

For all these reasons we chose another strategy to model our problem. Instead of using Newton-Euler equations for modeling the particles' motion and Stokes equations for the fluid flow, we use only the Stokes equations in the whole domain (including the interior of the particles). We take into account the presence of particles by using a second fluid with a high viscosity on which we impose a rigid body constraint. This type of strategy is widely used in the literature under the generic names of "penalty-like methods" or "fluid particle dynamics" [38–43].

In what follows, we describe briefly the basic ingredients of the FEM method as well as the penalty technique applied to our problem. To do this we need to recall some mathematical notations.

The fluid flow is governed by Stokes equations of an incompressible fluid that can be written as follows :

$$-\eta_0 \boldsymbol{\Delta}\mathbf{u} + \boldsymbol{\nabla} p = 0 \text{ in } V_f, \tag{2}$$

$$\boldsymbol{\nabla} \cdot \mathbf{u} = 0 \text{ in } V_f, \tag{3}$$

$$\mathbf{u} = \mathbf{u}^\infty \text{ on } \partial V_f. \tag{4}$$

Where :

- η_0, $\mathbf{u}$ and p are respectively the viscosity, the velocity field and the pressure.
- V_f is the domain occupied by the fluid. Typically $V_f = V \setminus B$ if we denote by V the whole domain and by B the rigid particles' domain,
- ∂V_f is the border of V_f,
- $\mathbf{u}^\infty$ is some given vector field for the boundary conditions (typically a velocity field representing the shear flow).

It is known that under some reasonable assumptions the problem (2)-(3)-(4) has a unique solution $(\mathbf{u}, p)$ [44].

As we will use the FEM for the numerical resolution of problem (2)-(3)-(4), we need to write its variational formulation. For sake of simplicity, we start by writing it in a standard way (fluid without particles), then we modify it using penalty technique to take into account the presence of particles. In what follows, we describe briefly these two methods, the standard variational formulation for the Stokes problem and the penalty technique to handle the rigid body motion of particles.

A. Variational formulations

The variational formulation of our initial problem (2)-(3)-(4) is given by : *Find* $(\mathbf{u}, p)$ *(see appendix of [45] for more details) such that :*

$$2\eta_0 \int_{V_f} \boldsymbol{\tau}(\mathbf{u}) : \boldsymbol{\tau}(\mathbf{v})\ dV - \int_{V_f} p\boldsymbol{\nabla}\cdot\mathbf{v}\ dV = 0, \forall \mathbf{v}, \tag{5}$$

$$\int_{V_f} q\boldsymbol{\nabla}\cdot\mathbf{u}\ dV = 0, \forall q, \tag{6}$$

$$\mathbf{u} = \mathbf{u}^{\infty} \text{ on } \partial V_f. \tag{7}$$

Where $\boldsymbol{\tau}(\mathbf{u})$ is the strain tensor

$$\boldsymbol{\tau}(\mathbf{u}) = \frac{1}{2}\left(\boldsymbol{\nabla}\mathbf{u} + (\boldsymbol{\nabla}\mathbf{u})^t\right) \tag{8}$$

and $\mathbf{v}$ and q are respectively the test functions for the velocity field $\mathbf{u}$ and the pressure p taken in some functional space (see [45]). As we have Dirichlet boundary conditions (7), $\mathbf{v}$ is supposed to vanish on ∂V_f.

The variational formulation (5)-(6)-(7) has the advantage to depend explicitly on $\boldsymbol{\tau}(\mathbf{u})$ which will be very useful to handle the rigid body motion. Note that this formulation is equivalent to the classical one thanks to the following identity

$$\int_{V_f} \boldsymbol{\tau}(\mathbf{u}) : \boldsymbol{\tau}(\mathbf{v})\ dV = \frac{1}{2}\int_{V_f} \boldsymbol{\nabla}\mathbf{u} : \boldsymbol{\nabla}\mathbf{v}\ dV \tag{9}$$

which holds for incompressible fluid. All details of calculations to obtain these variational formulations can be found in [45].

B. Penalty Method

We now briefly describe the penalty strategy in the framework of FEM method (see [38, 39] for more details).

The first step consists in rewriting the variational formulation (5)-(6)-(7) by replacing the integrals over the real domain occupied by the fluid ($V_f = V \setminus B$) by those over the whole domain V (including the particles B). It simply means that we extend the solution $(\mathbf{u}, p)$ to the whole domain V. More precisely, the penalty method replaces the particles by an artificial fluid with a high viscosity. This is made possible by imposing a rigid body motion constraint on the fluid that replaces the particles ($\boldsymbol{\tau}(\mathbf{u}) = 0$ in B). Obviously, the divergence free constraint is also insured in B. The problem (5)-(6)-(7) is then modified as follows : *Find* $(\mathbf{u}, p)$ *such that :*

$$2\eta_0 \int_{V} \boldsymbol{\tau}(\mathbf{u}) : \boldsymbol{\tau}(\mathbf{v})\ dV + \frac{2}{\varepsilon}\int_{B} \boldsymbol{\tau}(\mathbf{u}) : \boldsymbol{\tau}(\mathbf{v})\ dV - \int_{V} p\boldsymbol{\nabla}\cdot\mathbf{v}\ dV = 0, \forall \mathbf{v}, \tag{10}$$

$$\int_{V} q\boldsymbol{\nabla}\cdot\mathbf{u}\ dV = 0, \forall q, \tag{11}$$

$$\mathbf{u} = \mathbf{u}^{\infty} \text{ on } \partial V. \tag{12}$$

Where $\varepsilon \ll 1$ is a given penalty parameter.

Finally, if we denote the time discretization parameter by $t_n = n\delta t$, the velocity and the pressure at time t_n by $(\mathbf{u}_n, p_n)$, the velocity of a particle at time t_n by $\mathbf{W}_n$ and the position of its center by $\mathbf{X}_n$, we can write our algorithm as :

$$\mathbf{W}_n = \frac{1}{Volume(B)}\int_B \mathbf{u}_n\ dV \tag{13}$$

$$\mathbf{X}_{n+1} = \mathbf{X}_n + \delta t \mathbf{W}_n \tag{14}$$

$(\mathbf{u}_{n+1}, p_{n+1})$ solves :

$$2\eta_0 \int_V \boldsymbol{\tau}(\mathbf{u}_{n+1}) : \boldsymbol{\tau}(\mathbf{v})\, dV + \frac{2}{\varepsilon} \int_B \boldsymbol{\tau}(\mathbf{u}_{n+1}) : \boldsymbol{\tau}(\mathbf{v})\, dV - \int_V p_{n+1} \boldsymbol{\nabla} \cdot \mathbf{v}\, dV = 0, \tag{15}$$

$$\int_V q \boldsymbol{\nabla} \cdot \mathbf{u}_{n+1} dV = 0, \tag{16}$$

$$\mathbf{u}_{n+1} = \mathbf{u}^{\infty} \text{ on } \partial V. \tag{17}$$

This algorithm is valid for any dimension. Here, it has been implemented in $2D$ using a user-friendly FEM software `Freefem++` [46] (`http://www.freefem.org/ff++`).

III. RESULTS ON DISSIPATION AND EFFECTIVE VISCOSITY.

A. Particle-wall interaction - with a single wall.

In this section, we calculate the intrinsic viscosity $[\eta]$ defined above in eq.(1) for a dilute $2D$ suspension. To do so, we consider a single rigid circular particle in a confined shear flow (see figure 1). The shear rate $\dot{\gamma}$ is maintained to 1 for all the simulations. The whole mesh is composed by 8000 triangles and each particle is represented by approximately 70 elements. The velocity field $\mathbf{u}$ is approximated by finite elements of degree 2 ($\mathbb{P}_2$) and the pressure is approximated by linear finite elements ($\mathbb{P}_1$). Finally, we use free boundary conditions in x-direction.

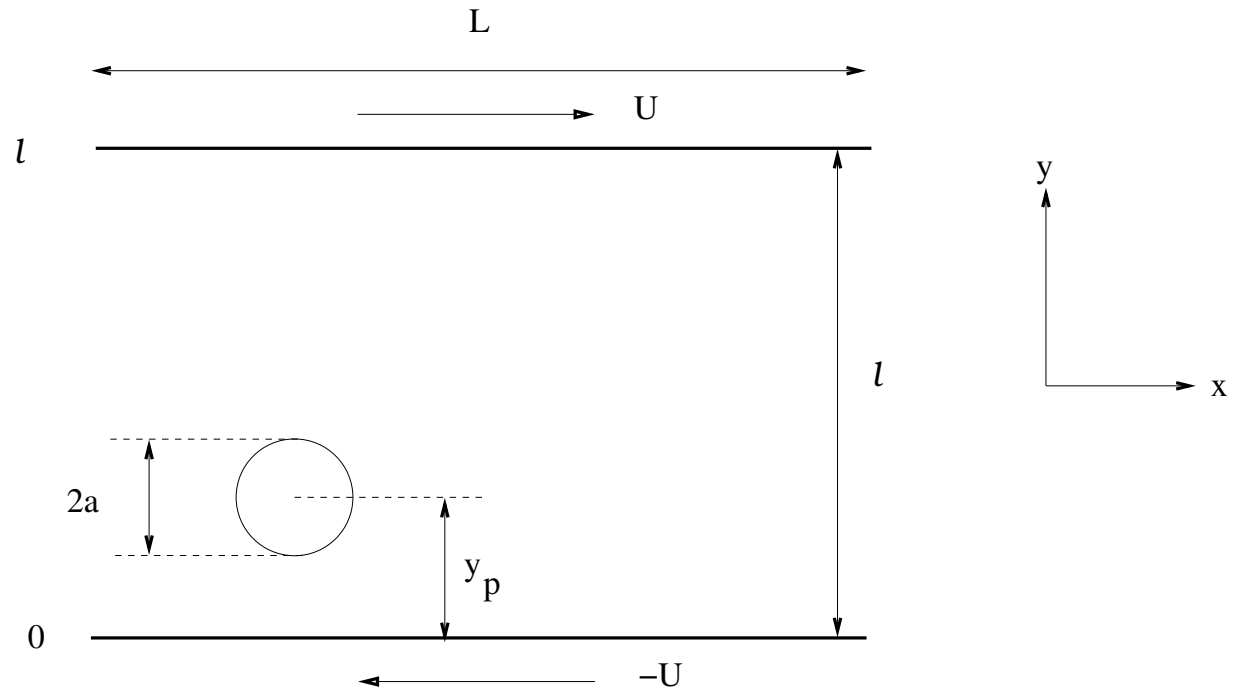

FIG. 1. A circular particle in a linear shear flow in presence of walls. Shear rate is $\dot{\gamma} = 2U/\ell$ and it is maintained to $\dot{\gamma} = 1$ in the simulations.

The box is large enough ($L/\ell = 60$) so that no boundary effects are present in $x-$direction, and the wall interdistance ℓ is varied in order to study the effect of the confinement. The volume fraction is then $\phi = \pi a^2/(L\ell)$. Since the $x-$dimension of the system is very long compared to the y one, the effective viscosity of this system should depend only on the dimensionless distance to the wall $\tilde{y} = y_p/\ell$ as well as on the confinement $C = a/\ell$. The total dissipation

is:

$$D = \frac{1}{2}\eta_0 \int_V \left|\boldsymbol{\nabla}\mathbf{u} + \boldsymbol{\nabla}\mathbf{u}^t\right|^2 \, dV, \tag{18}$$

where $\mathbf{u}$ is the velocity field in the fluid phase as well as in the particle. Inside particles, due to their solid motion, there is no dissipation and the integral holds on the whole domain (fluid and particles). In the spirit of homogenization, we consider an homogeneous Newtonian fluid of viscosity η_{eff}. The total dissipation is then:

$$D = \eta_{eff}\dot{\gamma}^2 L\ell. \tag{19}$$

The viscosity is obtained by equating eq.(18) and eq.(19), it gives:

$$\eta_{eff} = \frac{\eta_0}{2\dot{\gamma}^2 L\ell} \int_V \left|\boldsymbol{\nabla}\mathbf{u} + \boldsymbol{\nabla}\mathbf{u}^t\right|^2 \, dV. \tag{20}$$

And intrinsic viscosity is such that:

$$[\eta](\tilde{y}, C) = \lim_{\phi\to 0} \frac{\eta_{eff} - \eta_0}{\eta_0 \phi} \tag{21}$$

The problem is symmetrical with respect to the center of the channel ($\tilde{y} = 1/2$). Thus, we can restrict our study on the range: $\ell/2 < y_p < \ell - a$ (*i.e.* $1/2 < \tilde{y} < 1 - C$). The simulations consist in setting a particle at different $\tilde{y}$ in the channel in the range given above and calculate the effective viscosity.

Figure 2 shows the results for several distances to the wall and for several confinements. When the particle approaches the wall, the viscosity of the system increases. The rate of increase is higher when the particle is closer to the wall. For small confinement values, we recover $[\eta] = 2$ consistent with exact $2D$ values [35, 36]. For intermediate confinements, the viscosity is higher near the wall and decreases to $[\eta] = 2$ when approaching the center of the channel. It is interesting to note that for strong confinements, the viscosity never decreases to the limit $[\eta] = 2$ for a centered particle. This is due to the fact that for these confinements, the presence of walls cannot be neglected for any position of the particle.

For asymtotic cases (*i.e.* small confinements), it is possible to compare our numerical results to an analytical expression of $[\eta]$. We analytically calulate $[\eta]$ for a given distance between the particle and the wall. We made an expansion similar to the one done in [47] where we consider the problem of a single circular particle near a single wall. The fluid is considered as infinite along the $x-$direction and semi-infinite along y. One can expand the velocity field $\mathbf{u}(x, y)$ as a polynomial function of the dimensionless distance between the center of the particle and the wall: $h_0 = (\ell - y_p)/a = (1 - \tilde{y})/C$. The reflection method [47] is employed to satisfy boundary conditions at the wall. We find the solution for $\mathbf{u}$ by using eq.(21), we stop the expansion at the 6^{th} order and it reads (the expansion valid to order $o(1/h_0^{12})$ is given in Appendix D):

$$[\eta]_{1\,wall}(h_0) = 2 + \frac{2}{h_0^2} - \frac{1}{4h_0^4} + \frac{15}{16h_0^6} + o(1/h_0^6). \tag{22}$$

In figure 2, eq.(22) fits very well the numerical data for small confinements: the model is valid for confinements smaller than about $C \sim 0.065$.

For dilute suspensions, the contribution of each particle to $[\eta]$ is simply added. Thus, for a suspension of N similar particles of which positions are known, one can express the intrinsic viscosity of the whole suspension as:

$$[\eta](C) = \frac{1}{N}\sum_{i=1}^{N} [\eta](\tilde{y}_i, C), \tag{23}$$

where $\tilde{y}_i = y_{p,i}/\ell$ is the dimensionless vertical position of the i^{th} particle.

This first part of our work, allows us to see that the main contribution of each individual particle to the effective viscosity is due to the increase of dissipation between each particle and walls. We now examine denser suspensions, to understand the role of pairs of particles to the effective viscosity.

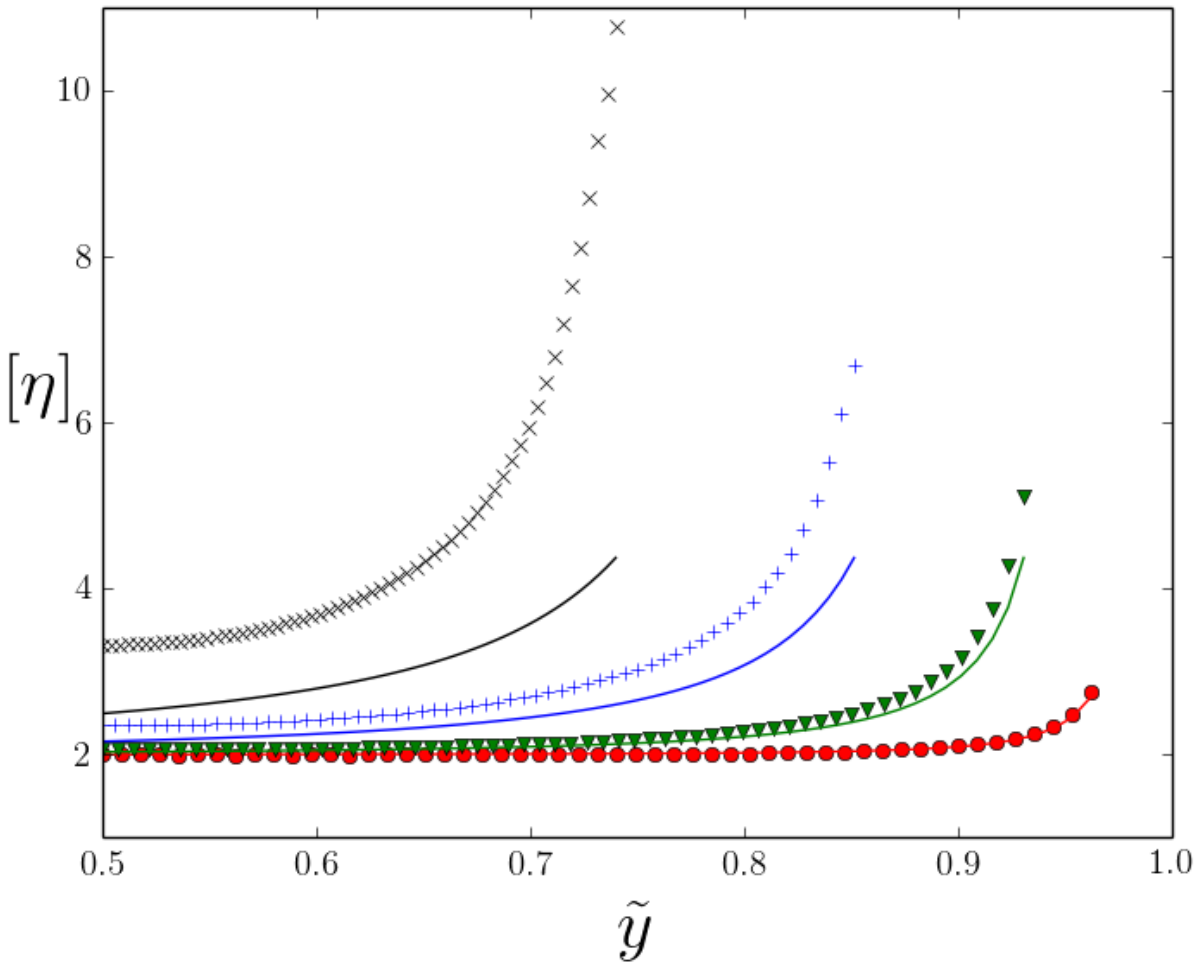

FIG. 2. Intrinsic viscosity depending on the dimensionless vertical position $\tilde{y}$ for several confinements. For small confinements, when the particle is close to the middle of the channel ($\tilde{y} \approx 0.5$) the asymptotic value $[\eta] = 2$ is recovered. For stronger confinements, even when the particle is centered ($\tilde{y} \approx 0.5$), we get $[\eta] > 2$. Red circles: $C = 0.022$, green triangles: $C = 0,0665$, blue +: $C = 0.143$, black x: $C = 0.25$. The analytical expansion [eq.(22)] (solid curves) fits quite well numercial results for small confinements ($C < 0.065$).

B. Particle-particle hydrodynamic interactions between two walls

Once increasing the volume fraction ϕ, hydrodynamic interactions between pairs of particles start to contribute to the effective viscosity [β term of eq.(1)]. In 3D, it was shown [19–21] that this contribution first decreases for intermediate confinements and even becomes negative for stronger confinements. As shown in this paper, the same effect arises in 2D.

We calculate the relative effective viscosity as a function of volume fraction for several values of confinement ranging from $C = 0.01$ to $C = 0.45$ (see figure 3 for some specific chosen confinement values). We clearly see a negative curvature of the curves $\eta_{eff}(\phi)$ for strong confinements. We fit these curves with a 2^{nd} order polynomial as in eq.(1) and obtain values of $[\eta]$ and β as a function of C. Note that we do this fit for values of ϕ below $\phi_{max} = 12\% \pm 2\%$ where no third order contribution in ϕ are necessary to fit the data. We vary a bit ϕ_{max} from 10% to 14% as well as particle configurations in order to evaluate the uncertainty on $[\eta]$ and β. On figure 4, we see the increase of $[\eta]$ as a function of C and the decrease of β as well as its sign change for strong confinements. Note that for stronger confinements, β re-increases to 0 asymptotically. For small confinement values (i.e. $C = a/\ell \to 0$) we asymptotically reach the following values for an infinite fluid $[\eta]_\infty = 2$ and $\beta_\infty = 3.6 \pm 0.1$. These numerical values are in perfect agreement with the reported value of the literature: $[\eta]_\infty = 2$ in $2D$ [35, 36] and with our own analytical result $\beta_\infty = 3.6$ (see appendix C).

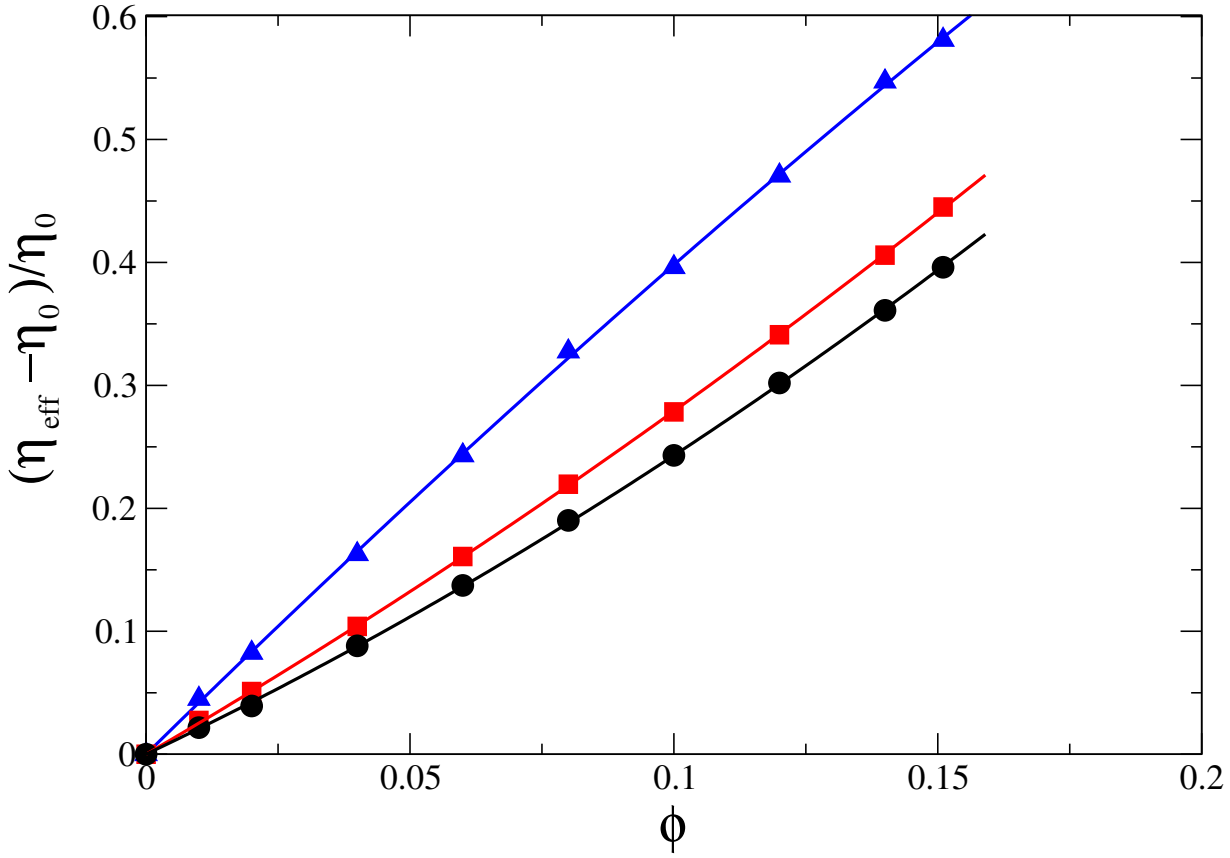

FIG. 3. Relative effective viscosity as a function of the volume fraction ϕ for several values of confinements: $C = 0.01$ (black circles), $C = 0.13$ (red squares) and $C = 0.286$ (blue triangles). Solid curves are the fits done with eq.(1). For $C = 0.01$, $[\eta] = 2.0$ and $\beta = 3.6$. For $C = 0.12$, $[\eta] = 2.4$ and $\beta = 3.2$. For $C = 0.3$, $[\eta] = 4.2$ and $\beta = -2.0$ We clearly see an increase of intrinsic viscosity $[\eta]$ (slope at the origin) and a decrease and even a negative value of the curvature β when increasing confinement.

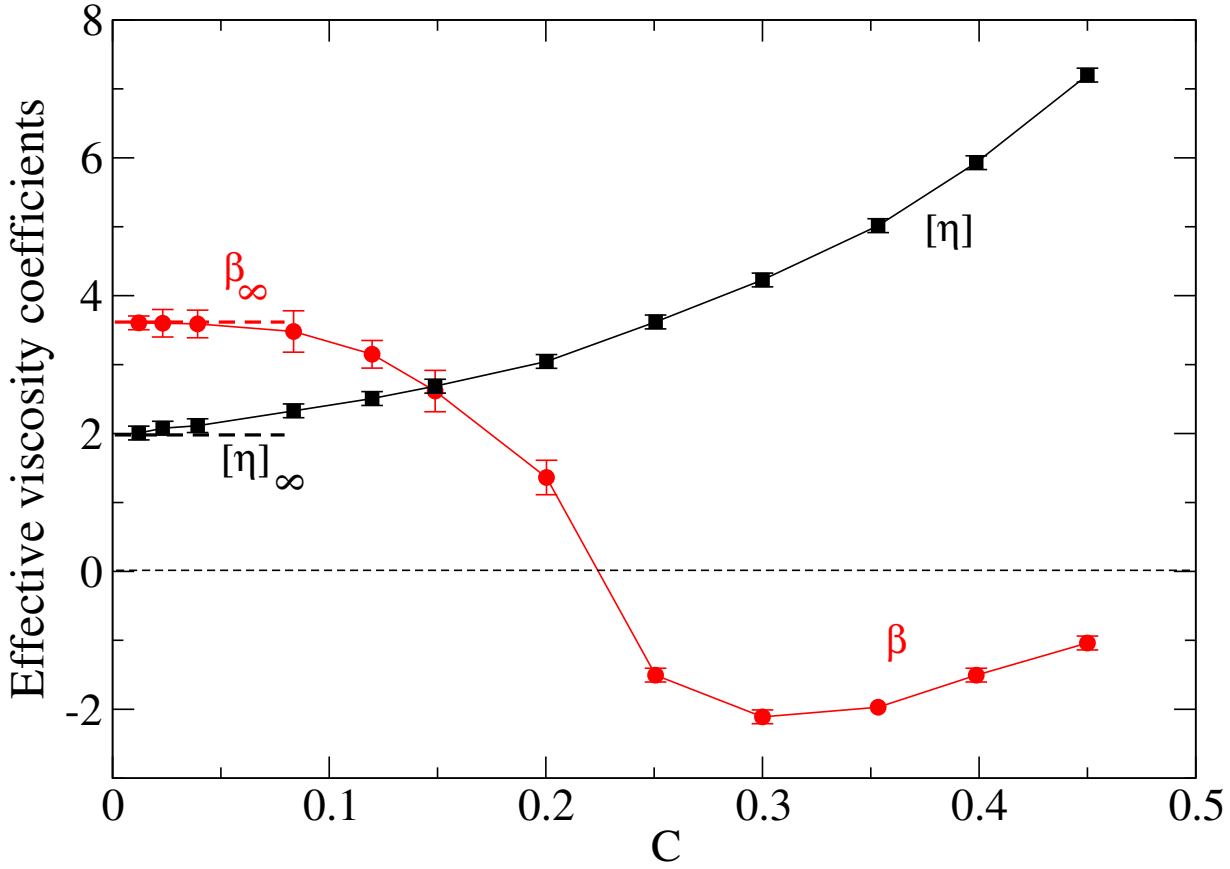

FIG. 4. Parameters $[\eta]$ (black squares) and β (red circles) as a function of confinement C. The error bars are calculated from several fits done with different maxima of the volume fraction (see text). Values of $[\eta]_\infty$ and β_∞ are indicated by horizontal dashed lines.

Since it is much more convenient to represent the velocity field in $2D$ as well as the dissipation density, we can easily give an interpretation of our results. Figure 5 shows the dissipation density field $\delta = \frac{1}{2}\eta_0 \left|\boldsymbol{\nabla}\mathbf{u} + \boldsymbol{\nabla}\mathbf{u}^t\right|^2$ for a suspension of particles that are randomly distributed between the walls. Dissipation density around a single disk has a $\cos(4\theta)$ angular distribution (see appendix A) with maxima around $\pi/4$ (mod $\pi/2$). Therefore, it is not surprising that each pair of particles dissipates energy with the same kind of symetry *i.e.* along the axis of extension/compression of the shear flow, *i.e.* at 45° (mod 90°) [see Fig.(5)]. Along x and y, pairs dissipate much less.

Then, by increasing the confinement, we observe an increase of dissipation between each particle and walls (see figure 6) and a decrease of dissipation between particles since the number of configurations with two close particles at 45° (mod 90°) obviously decreases while the number of configurations of aligned particles along x-axis increases for higher confinements. Thus, by increasing C, particle-wall dissipation tends to increase the intrinsic viscosity $[\eta]$ since it is due to each individual particle while dissipation inside pairs tends to decrease the contribution of HI to the effective viscosity and makes β decrease. Now, we are going to examine the dissipation and the dissipation density around a pair of particles in order to understand why the β term is becoming negative above a given confinement *i.e.* when particles are aligned along the flow.

In order to evaluate the dissipation D as a function of the pair orientation in the shear flow, we consider two confined particles and we vary the angle θ between the line joining each particle center and the x-axis (see figure 7). We calculate the dissipation D on the whole simulation box by using eq.(18). Since $\eta_{eff}(\phi) = D/(\dot{\gamma}^2 L\ell)$, by using eq.(1) and eq.(23) to calculate $[\eta]$, we can calculate β as a function of the angle θ. It confirms (figure 8) that the maximum of dissipation (*i.e.* maximum of effective viscosity) occurs at 45° (when this configuration is possible according to the confinement value). Figure 8 also highlights that when particles are close to alignment *i.e.* for $\theta < 20°$ and $\theta > 160°$, negative values of β are obtained. Note that for $80° < \theta < 100°$, we also obtain a negative value for β but much smaller than for aligned particles. Another way to visualize the dip of dissipation is to compute the dissipation as a function of disk separation $\mathbf{r}(x, y)$ in non-confined situation (fig.9) from the analytical expression (see appendix B). It is clear that for particles aligned along x or y, the dissipation between the disks is smaller than

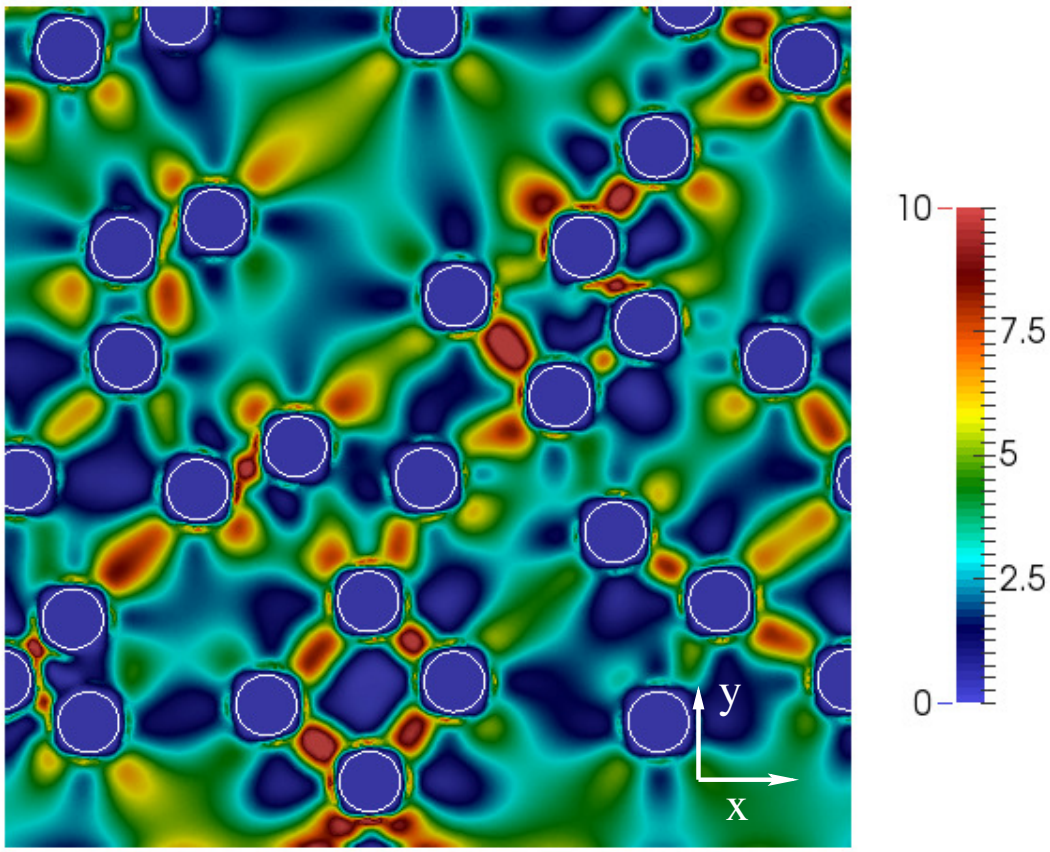

FIG. 5. Dissipation density for a given particle configuration for $C = 0.012$ (partial view of the simulation box). Dissipation is strong between close particles at 45°. The color scale indicates dissipation values on an arbitrary scale from 1 to 10. Density of dissipation without particles is 3.

the dissipation without particles. The presence of walls forces the particles to be aligned along x.

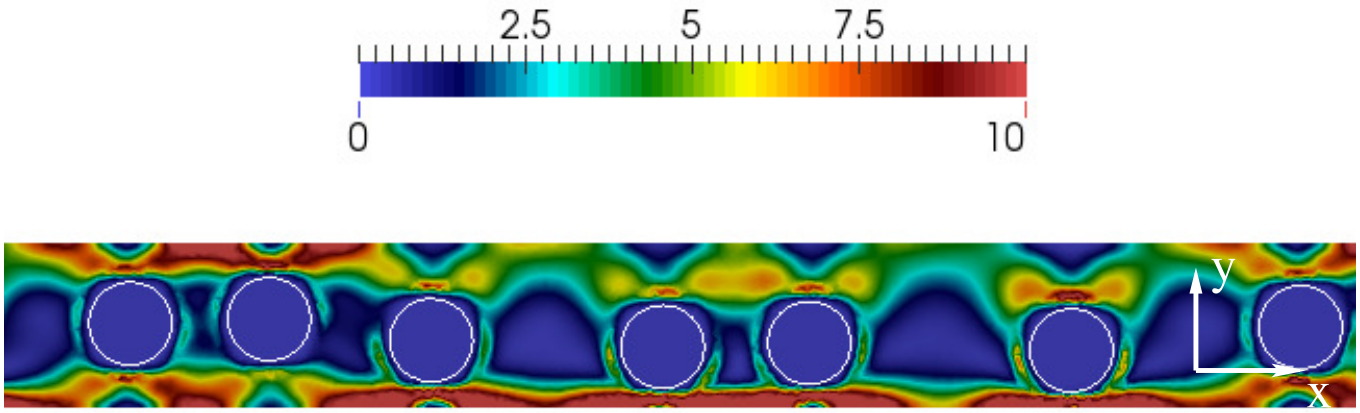

FIG. 6. Dissipation density for a given particle configuration for $C = 0.25$ (partial view of the simulation box along x). Dissipation is stronger between particles and walls and there are less particles at 45° due to the confinement. Note the "dips" of dissipation between particles. The color scale indicates dissipation values on an arbitrary scale from 1 to 10. Density of dissipation without particles is 3.

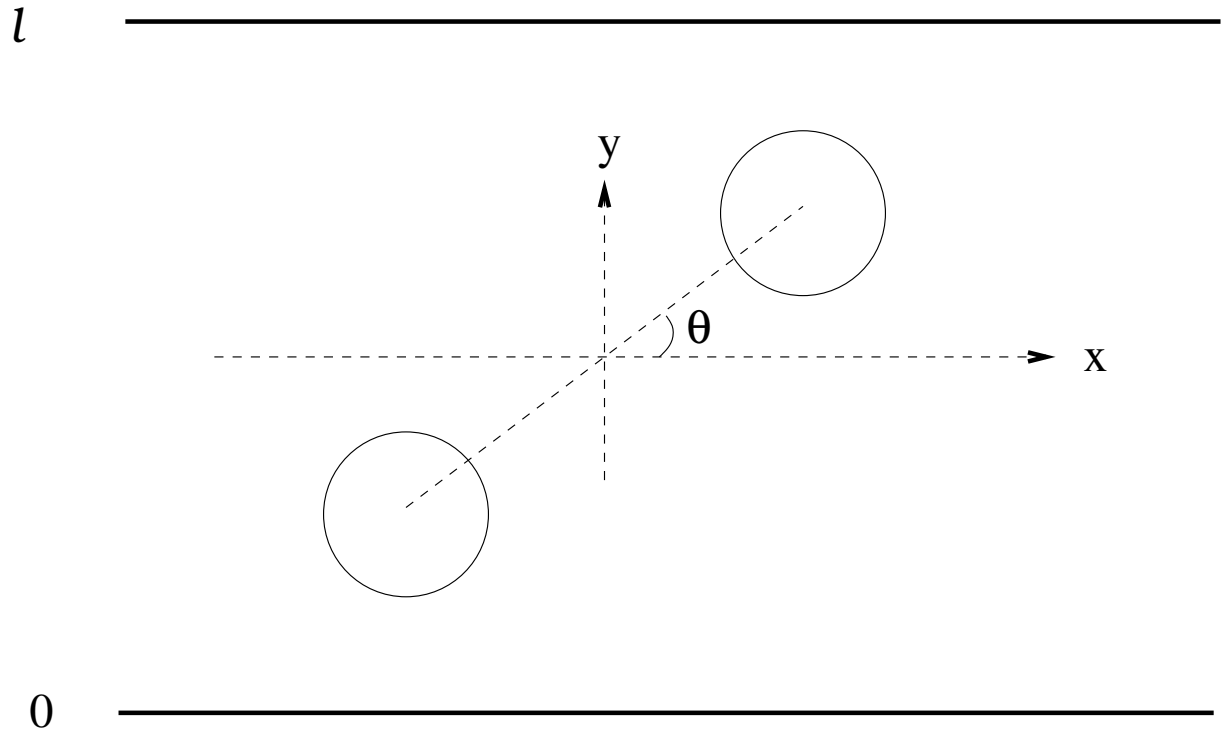

FIG. 7. A pair of particles, the line joining their centers makes an angle θ with the $x-$axis. Dissipation is integrated inside the whole simulation box and θ is varied.

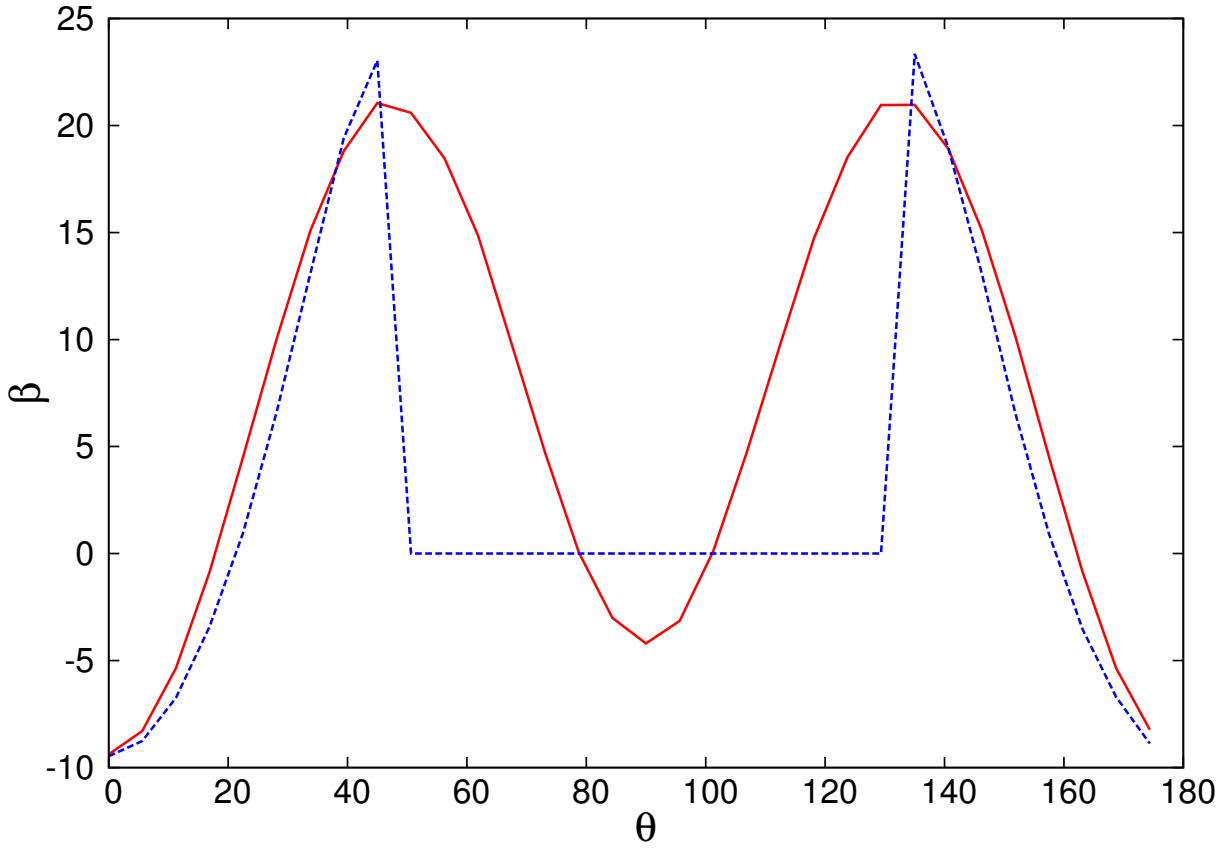

FIG. 8. Parameter β in the case of two disks as a function of θ, for $C = 0.25$ (red solid curve) and $C = 0.29$ (blue dashed curve). Note the negative values of β (see text).

These results are supported by the visualization of the dissipation density and stream lines around the particles. For a pair of particles at 45° we observe an increase of dissipation density between the particles (fig. 10-a). It is due to two vortices which rotate in the same direction (fig. 10-b) . It creates a zone of strong shear at their intersection which dissipates a lot.

For a pair aligned along the flow (*i.e.* along the $x-$axis), we observe the formation of a compression/extension flow between the two particles (see figure 11-b) in the dip of dissipation density.

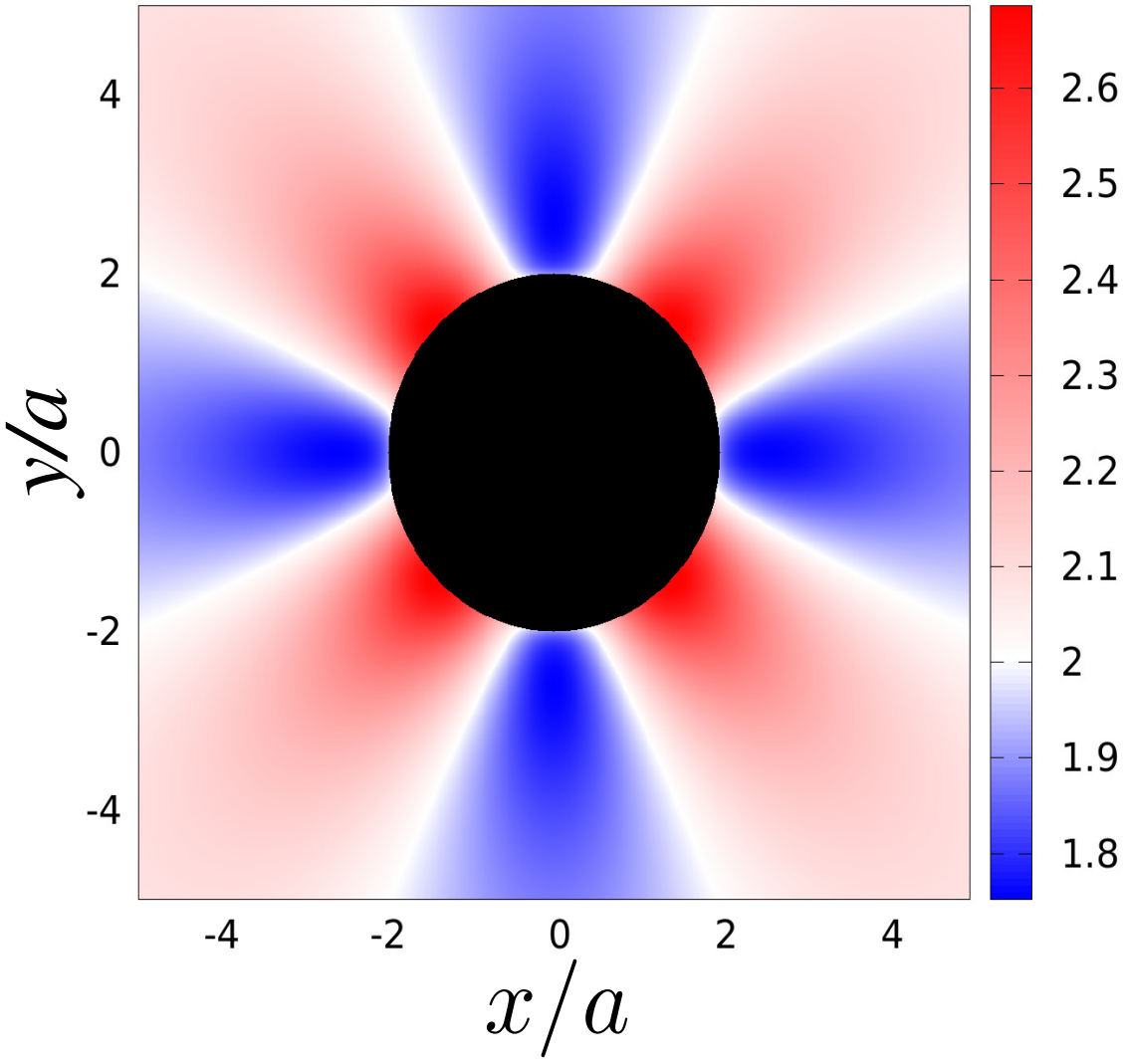

FIG. 9. Dissipation corresponding of two disks as a function of the disk separation $\mathbf{r}(x, y)$ for $C \to \infty$ (see appendix B). Dissipation in absence of particle is 2.

The dissipation density between two aligned particles δ_{loc} is smaller than the backbround density dissipation, (*i.e.* the dissipation of the flow without particles $\delta_0 = \eta_0 \dot{\gamma}^2$). The origin of this local decrease of dissipation density is due to the slow-down of angular velocity Ω of the particles when aligned due to their mutual HI (see figure 12): rotation of each particle slows-down rotation of its aligned neighbour. This slow-down leads to a screening of the imposed shear rate and of the associated dissipation density between two aligned particles. Note that in figure 12 particles are weakly confined ($C = 0.04$). It has been shown before [21] that the confinement also decreases the angular velocity of each particle. This tends to increase the screening effect of the imposed shear rate between aligned particles. On the contrary, when particles are close enough but $y-$shifted, their angular velocity is bigger than when they are far apart (see figure 12).

The fluid region between two aligned and close particles having a smaller dissipation than the one imposed by the motion of walls without particles, represents a "dip of dissipation" which contributes to decrease the total dissipation for aligned pairs of particles compared to two isolated single particles. Indeed, on figure 13, we can observe the evolution of the dissipation density profile between two particles in a shear (the pair being aligned along the flow). A dip of dissipation is created between the particles and increases when the two particles get closer. This explains why the pair interaction (when the pair of particles is aligned along the flow) contributes negatively to the effective viscosity. Note that the confinement is weak in figure 13, somehow the confinement forces the aligned configuration where dips of dissipation occur and makes β decrease to negative values.

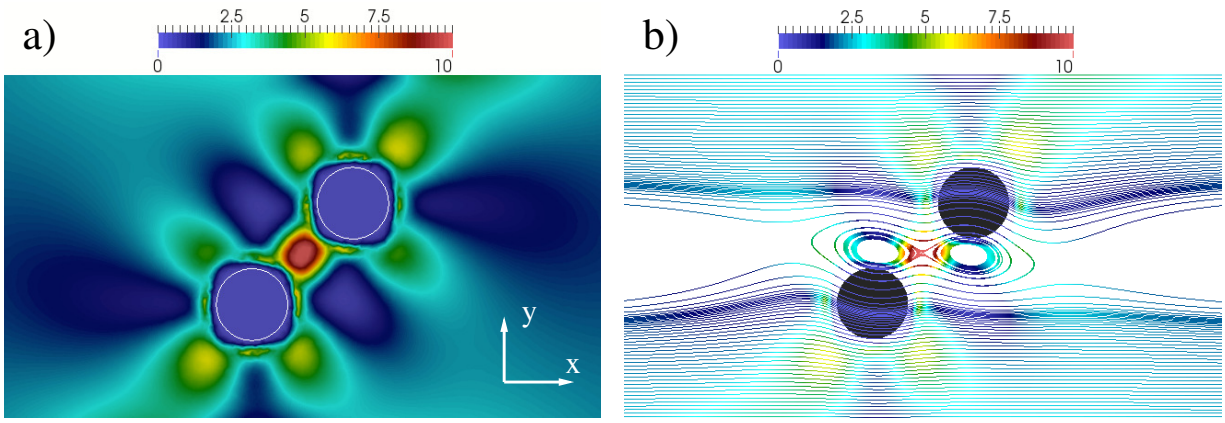

FIG. 10. a) Dissipation density and b) current lines and dissipation between two weakly-confined particles (colored in black) positioned at 45° with $C = 0.044$ (partial view of the simulation box). The color scale indicates dissipation values on both figures. Density of dissipation without particles is 3.

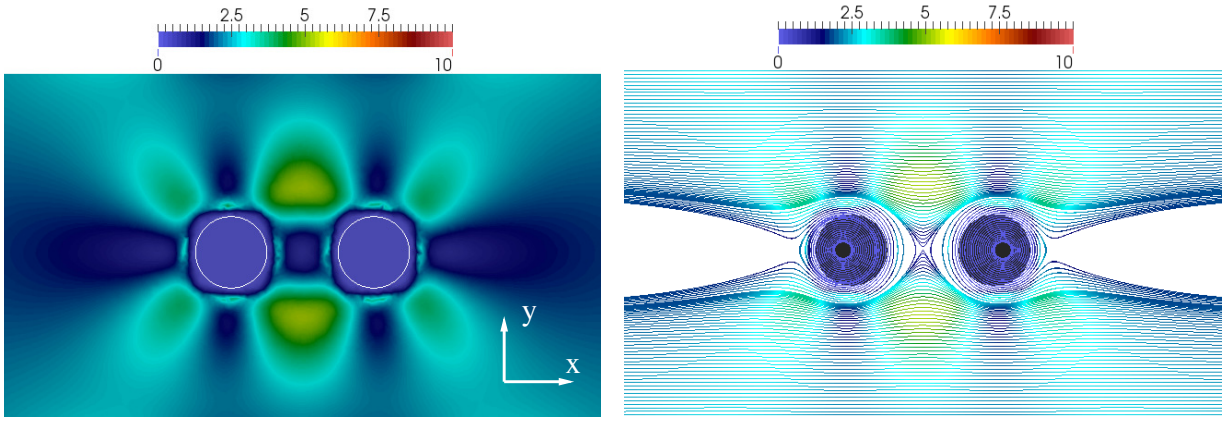

FIG. 11. a) Dissipation and b) current lines and dissipation between two weakly confined and aligned particles (colored in black) with $C = 0.044$ (partial view of the simulation box). The color scale indicates dissipation values in both figures. Density of dissipation without particles is 3. Dissipation is clearly weaker than in the case of particles positioned at 45° (fig. 10).

The re-increasing of β as a function of C (figure 4) is explained by the fact that when confinement is increased, the relative distance between particles increases in order to stay in the limit $\phi < 12\%$. Therefore, the contribution of HI between particles decreases ($\beta \to 0$).

C. Comparison with the 3D case.

In order to confirm our observations in $2D$, we made simulations in $3D$ which are much less convenient to perform because of the time and memory consumption as well as the flow field representation. In figure 14, we have schematically represented two confined spheres located in a plane parallel to the walls.

This is the situation which is relevant for confined configurations. The line joining the spheres makes an angle φ with the shear plane (xOz plane). In figure 15-a, we set two aligned spherical particles in the shear plane ($\varphi = 0°$) and calculate their dissipation density in the plane containing the sphere centers (xOy). Here also, a dip of dissipation is obtained between the two particles (see figure 15-a). When the line joining the two confined particles makes an angle $\varphi = 45°$ with the shear plane (see figure 15-b), no increase of dissipation density is observed between the particles. And when $\varphi = 90°$, a maximum of dissipation density is observed between the two particles (see figure 15-c). But a careful averaging on the different configurations (*i.e.* from $\varphi = 0°$ to $\varphi = 180°$) shows that the contribution of aligned particles dominates and leads to a decrease of dissipation for confined pairs of particles. So, even if $3D$ simulations

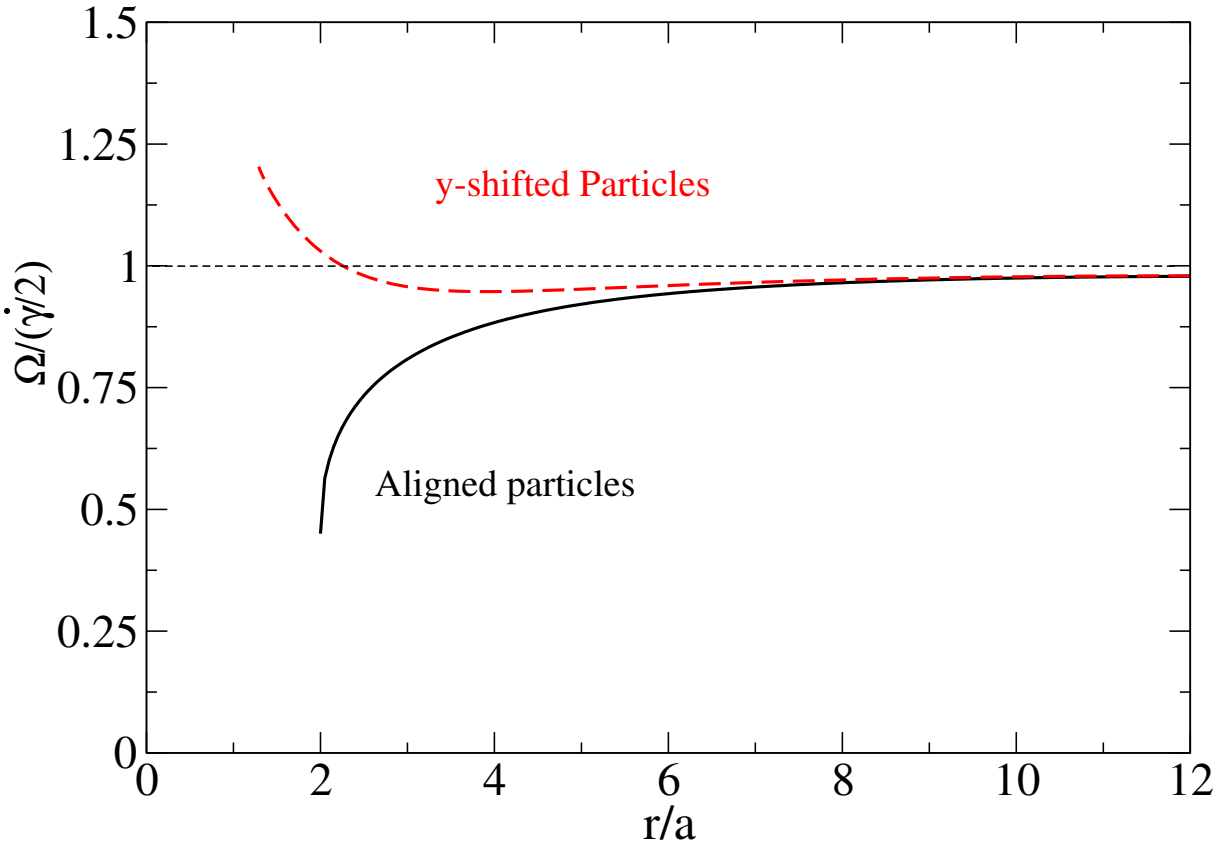

FIG. 12. A pair of particles within a shear flow. Angular velocity Ω of each particle divided by $\dot{\gamma}/2$ is plotted as a function of the particle interdistance $r/a = (x^2 + y^2)^{1/2}/a$. While y is fixed, x is varied. Red dashed curve: shifted particles along y. Particles are symmetrically shifted from the center of the flow, their y-interdistance is $2.5a$. Black solid curve: aligned particles along x ($y = 0$, $\theta = 0°$). Note that for large interdistances, in both cases Ω does not tend to $\dot{\gamma}/2$ but to a slightly smaller value. This is due to the confinement effect (here $C = 0.044$).

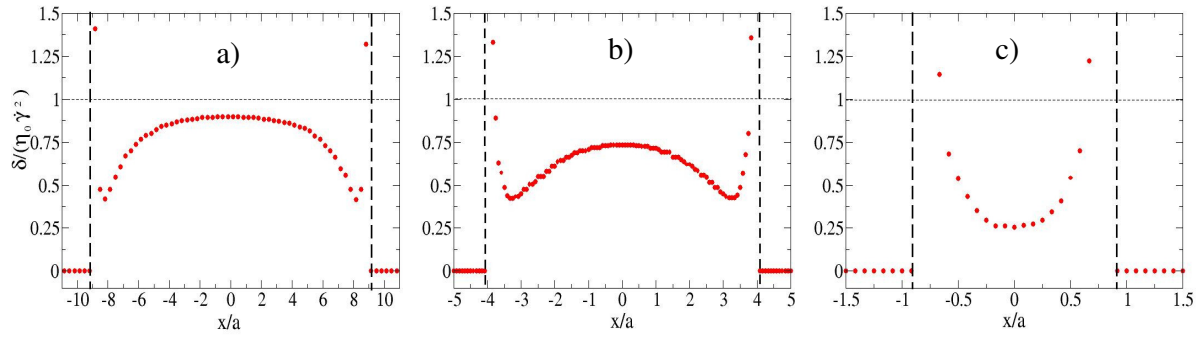

FIG. 13. Dissipation density δ between two aligned particles along the x-axis divided by $\eta_0\dot{\gamma}^2$ (*i.e.* the dissipation density far from the particles). Here $C = 0.04$. The vertical dashed lines indicate the interfaces of particles where $\delta = 0$ inside. The particle interdistance x (since $y = 0$) is taken between particle centers. a) $x/a = 20.3$, b) $x/a = 10.2$ and c) $x/a = 3.6$. We clearly see that the dip of dissipation between the particles is enhanced when particles are closer.

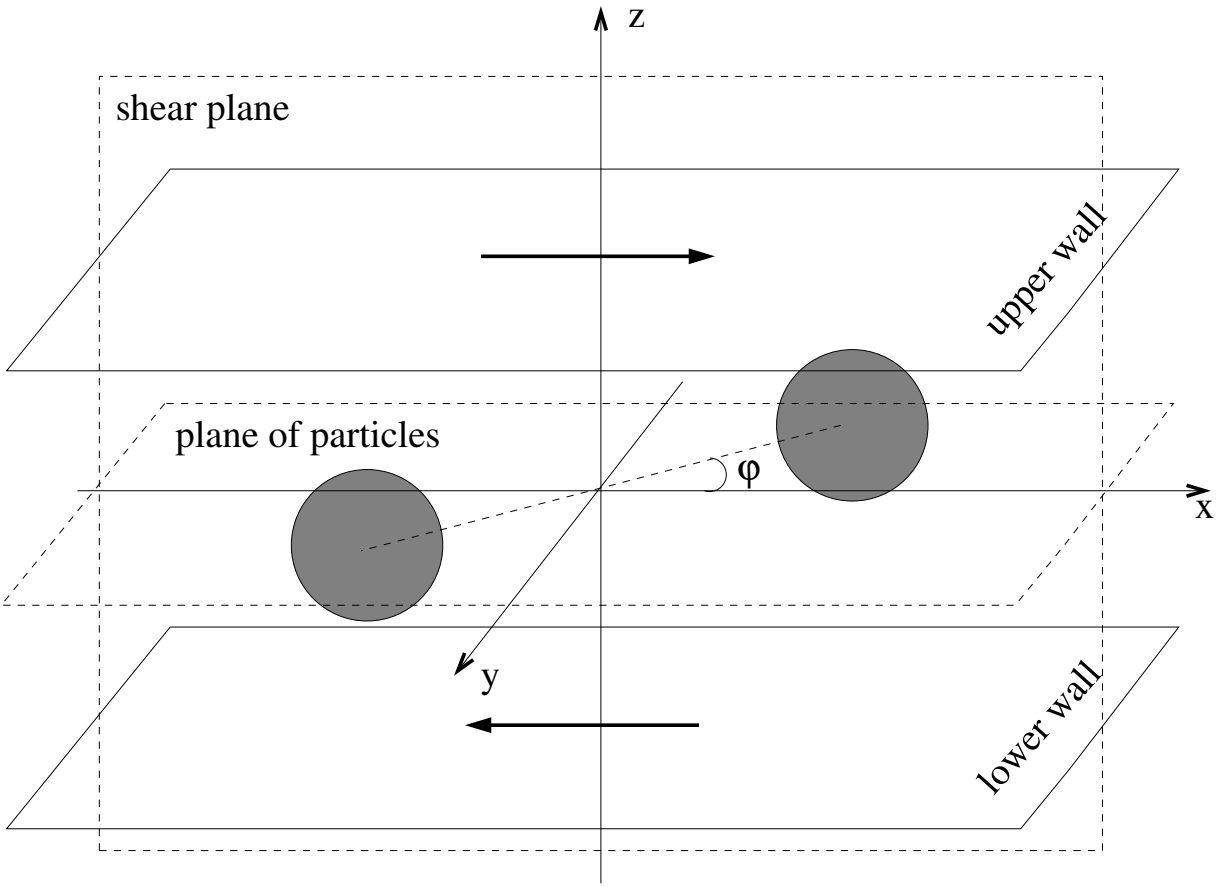

FIG. 14. Two spheres confined in a shear flow. The spheres are in the same plane parallel to the walls.

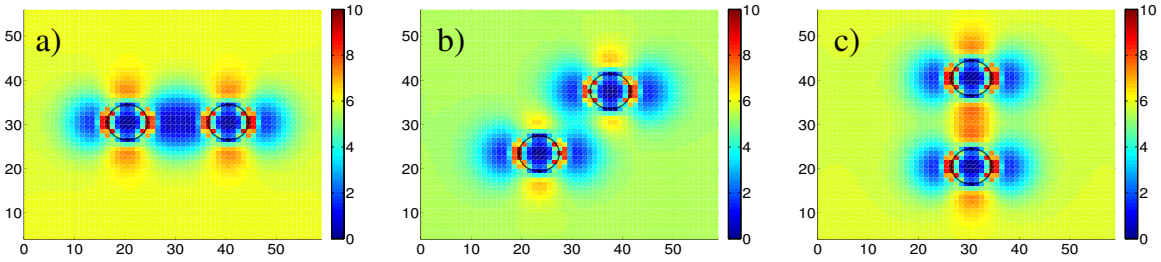

FIG. 15. Dissipation density in the $x0y$ plane between two particles as a function of φ for a confinement ($C = 0.25$). a) $\varphi = 0°$, b) $\varphi = 45°$ and c) $\varphi = 90°$. Non-uniform dissipation field inside particles is due to discretization effect.

require additional unavoidable averagings on different configurations, we see that qualitatively the same interpretation can be found in $3D$ and in $2D$.

IV. CONCLUSIONS.

In this paper we calculate the intrinsic viscosity $[\eta]$ and the contribution of hydrodynamic interactions β to the effective viscosity of a confined $2D$ suspension. For the less confined case ($C = 0.01$) we obtain the values $[\eta] = 2.0$ and $\beta = 3.6 \pm 0.1$ very close to the analytical values for an infinite fluid, *i.e.* $[\eta]_\infty = 2$ and $\beta_\infty = 3.6$. Even for a non-confined suspension the value $\beta_\infty = 3.6$ is not referenced in the literature. We show that the confined

$3D$ suspension rheology can be clarified with the help of $2D$ simulations. The visualization of the entire flow in $2D$ combined with the calculation of dissipation allows to understand why intrinsic viscosity $[\eta]$ increases with the confinement: regions of fluid squeezed between particles and walls have a high dissipation density. Our simulations also explain why the HI contribution of pairs of particles to the effective viscosity decreases with confinement and becomes negative: dips of dissipation are created between close particles aligned along the shear flow. This effect is caused by the slow-down of angular velocity of close and aligned particles. The confinement helps to force the particles in that specific configuration but similar results are obtained for non-confined but aligned particles. $3D$ simulations confirm the interpretation deduced from the $2D$ results. If $2D$ models cannot of course replace $3D$ ones, we believe that the combination of both approaches can help to clarify some specific points at least qualitatively. $2D$ simulations are usually faster, and easier to implement and very convenient for data visualization. They can serve as a very efficient tool for the development of $3D$ simulations and for their understanding but are also an important tool to understand hydrodynamic interactions between bio-entities generally embedded in fluid bio-membranes.

V. ACKNOWLEDGEMENTS.

This work has been supported by the LabEx Tec 21 (Investissements d′Avenir - grant agreement ANR-11- LABX-0030) and the ANR project Vivabrain - grant agreement ANR-12-MONU-0010.

Most of the computations presented in this paper were performed using the Froggy platform of the CIMENT infrastructure `https://ciment.ujf-grenoble.fr`, which is supported by the Rhône-Alpes region (GRANT CPER07_13 CIRA) and the EquipMeso project (ANR-10-EQPX-29-01).

A.F. acknowledges financial support from CNES (Centre National d′Etudes Spatiales) and ESA (European Space Agency).

Appendix A: Single disk in shear flow

The problem of a single disk in shear flow can be fully solved analytically. In this and the following appendices, we use the coordinate system (x,y) such that the shear flow is written as $\boldsymbol{v}^\infty(x,y) = \dot\gamma \boldsymbol{e_x} y$. For convenience, we represent 2D vectors as complex numbers in order to simplify the notation. For example, the position will be written as $\zeta = x + iy$ and the velocity $\boldsymbol{u}(x,y)$ will be written as $\xi(\zeta) = u_x(x,y) + iu_y(x,y)$. It is generally known[48], that a solution of Stokes equations (2, 3) can be written as

$$\xi(\zeta) = A(\zeta) - \zeta\overline{A'(\zeta)} + B(\overline{\zeta}), \tag{A1}$$

where $A(\zeta)$ and $B(\zeta)$ functions that are analytical inside the fluid and the upper bar stands for the complex conjugate. The undisturbed shear flow is written as

$$u_x^\infty(x,y) + iu_y^\infty(x,y) = \frac{\dot\gamma(z-\overline{z})}{2i}. \tag{A2}$$

Placing a ridid disk of radius a in the origin results in the following expression of the flow outside the disk

$$\xi(\zeta) = \frac{\dot\gamma(z-\overline{z})}{2i} - \frac{i\dot\gamma a^2}{2z} + \frac{i\dot\gamma a^2 z}{2\overline{z}^2} - \frac{i\dot\gamma a^4}{\overline{z}^3}. \tag{A3}$$

It is easy to check that expression (A3) is of form (A1) and that the velocity at the disk boundary corresponds to rotation with angular velocity $-\dot\gamma/2$. The dissipation density δ corresponding to the flow (A3) is

$$\begin{aligned}\delta(\zeta) = \dot\gamma^2\eta_0\Bigg(1 + 4\frac{a^4}{|\zeta|^4} - \frac{12a^6}{|\zeta|^6} + \frac{9a^8}{|\zeta|^8} - \\ - \frac{2a\zeta}{\overline{\zeta}^3} - \frac{2a^2\overline{\zeta}}{\zeta^3} + \frac{3a^4}{\zeta^4} + \frac{3a^4}{\overline{\zeta}^4}\Bigg).\end{aligned} \tag{A4}$$

Writing $\zeta = |\zeta|e^{i\alpha}$, we observe that the angular dependence of δ has the form of $\delta(\zeta) = \delta_0(|\zeta|) + \delta_4(|\zeta|)\cos 4\alpha$.

Appendix B: Hydrodynamic interaction of two disks in unconfined shear flow

In order to calculate the the Batchelor coefficient for a 2D suspension of rigid disks, it is first necessary to evaluate the hydrodynamic interactions of two disks as a function of the vector $\boldsymbol{r}$ separating their centers. For convenience, we put the particles in positions $\boldsymbol{r}/2$ and $-\boldsymbol{r}/2$. The symmetry of the problem dictates that $\xi(\zeta) = -\xi(-\zeta)$. The flow disturbance $\xi_1(\zeta)$ due to a force-free disk with the center at position $\zeta_0 = (r_x + ir_y)/2$ can be written as a multipolar expansion

$$\xi_1(\zeta + \zeta_0) = \sum_{k=1}^{\infty} \frac{A_k}{\zeta^k} + \frac{k\overline{A_k}\zeta}{\overline{\zeta}^{k+1}} + \frac{B_k}{\overline{\zeta}^k}. \tag{B1}$$

The expansion (B1) converges everywhere for $|\zeta| > a$ (a being the disk radius as defined above), including infinity, where the flow disturbance is equal to zero. Were there a force acting on the disk, the expansion (B1) would contain a logarithmic singularity in the disk center. Accounting for the symmetry of the problem, the velocity disturbance due to the second disk can be expressed as $\xi_2(\zeta) = -\xi_1(-\zeta)$. The total flow field outside of the disks is the sum of the flow disturbance due to each disk and the unperturbed shear flow at infinity $\xi^\infty = i\dot\gamma(\overline{\zeta} - \zeta)/2$:

$$\xi(\zeta) = \xi_1(\zeta + \zeta_0) - \xi_1(-\zeta - \zeta_0) + \xi^\infty(\zeta). \tag{B2}$$

The coefficients A_k, $k > 0$ and B_k $k > 1$ are calculated from the no-slip boundary condition at the disks' boundaries

$$\xi(\zeta_0 + ae^{i\sigma}) = \xi_0 + i\Omega e^{i\sigma}, \tag{B3}$$

where $\sigma \in \mathbb{R}$ is the parametrization of the boundary of the disk, ξ_0 is the velocity of the disk located at $\boldsymbol{r}/2$ and Ω is its angular velocity. The condition of (B3) is reduced to a discrete (albeit infinite) linear system by projecting on the space of Fourier harmonics $e^{ik\sigma}$. This system is closed by the zero-torque condition $\Im B_1 = 0$. The resulting system is solved for the approximate values of A_k and B_k by assuming that each unknown has an analytical expansion in powers of the small parameter $2a/r$. Truncating all calculations to a proper degree of $2a/r$ allows us to calculate the coefficients in each expansion. We do not give here the resulting calculations. Instead, we list below several first terms in the expansion for each parameter of interest, which can serve as a basis of an independent validation of our study. The parameters of interest are the the velocity ξ_0, the angular velocity Ω, and the coefficient A_1. The latter is closely related to the stress generated in suspension. In particular, $-4\Im A_1/(S\dot\gamma)$ is the contribution of the particle to the effective viscosity of the suspension, as will be explained in the next section. In figure (9) this contribution is integrated over S which gives a quantity proportional to dissipation. Here S refers to the total area occupied by the suspension, as defined above.

$$\Re\xi_0^{PW} = \dot\gamma\left[\frac{r\sin\theta}{2} - \frac{a^2(\sin 3\theta + \sin\theta)}{2r} + \frac{a^4(\sin 3\theta - 2\sin\theta)}{2r^3} + o(a/r)^3)\right], \tag{B4}$$

$$\Im\xi_0^{PW} = \dot\gamma\left[\frac{a^2(\cos 3\theta - \cos\theta)}{2r} - \frac{a^4(\cos 3\theta + 2\cos\theta)}{2r^3} + o((a/r)^3)\right], \tag{B5}$$

$$\Omega^{PW} = \dot\gamma\left[-\frac{1}{2} + \frac{a^2\cos 2\theta}{2r^2} - \frac{2a^4\cos 2\theta}{r^4} + o((a/r)^4)\right], \tag{B6}$$

$$\Re A_1^{PW} = \dot\gamma\left[-\frac{a^4\sin 4\theta}{r^2} + \frac{3a^6\sin 4\theta}{r^4} + o((a/r)^4)\right], \tag{B7}$$

$$\Im A_1^{PW} = \dot\gamma\left[-\frac{a^2}{2} - \frac{a^4\cos 4\theta}{r^2} - \frac{a^6(2 + 3\cos 4\theta)}{r^4} + o((a/r)^4)\right], \tag{B8}$$

Here all expressions refer to the disk located at $\boldsymbol{r}/2$ and the superscript PW is added to stress that the values are calculated for the pairwise interaction of two disks.

Appendix C: Viscosity of a semi-dilute suspension

The effective viscosity of a semi-dilute suspension has been calculated for force-free spheres on several occasions[3, 32]. Because the present problem is quite similar to the 3D case, we shall only briefly discuss the main steps in the derivation and then provide the final answer. As shown in [49], the effective viscosity of a suspension of force-free particles can be calculated as

$$\eta = \eta_0 + \frac{1}{S\dot{\gamma}} \sum_\alpha \int_{\Gamma_\alpha} f_x y ds = \eta_0 - \frac{4\pi\eta_0}{S\dot{\gamma}} \sum_\alpha \Im A_1(\alpha), \tag{C1}$$

where α indexes all particles, Γ_α is the contour of the particle α, $\boldsymbol{f}ds$ is the sum of forces acting from the infinitesimal arc of length ds on the particle boundary. This force acts both on the fluid surrounding the particle, creating the flow disturbance, and inside the particle, in a way that cancels the imposed shear flow and the flow due to the other particles. The second equality in (C1) is easy to check for circular objects considered here but its validity is independent of particle shapes. The value A_1 for a given particle depends, generally speaking, on the states and relative positions of all other particles. Therefore, an averaging of some form is required to obtain a closed-form solution. Inasmuch as we are interested in the ϕ^2 coefficient of the viscosity expansion in powers of the concentration ϕ, only pair-wise interactions of the disks have to be considered in our calculation. The main difficulty here is, however, that the integral of (B8) over all possible relative orientations of the two disks does not converge absolutely [3, 32]. We trace this difficulty to the fact that eq. (B8) was derived assuming that the distance r between the disks be much smaller than the size of the region where the shear flow is imposed. Now if we allow the relative distance between two disks to go to infinity when averaging expression (B8), this assumption will no longer be satisfied. We overcome this problem by first using the mean-field approximation, similarly to the method used in [3].

In the mean-field approximation, we consider a disc D immersed in a dilute suspension of weakly-interacting rigid disks. That is, (i) relative positions of the disks are not correlated and they can even overlap with each other and (ii) all disks have the same (but yet unknown) distribution of forces, which arise from the imposed flow and the hydrodynamic interaction with the other disks. Our plan is to calculate the viscosity of a semi-dilute suspension of disks in the mean-field approximation and then to apply the corrections accounting for the fact that disks can not overlap and for the properly calculated hydrodynamic interactions of two disks. In the mean-field approximation, each disk is suspended in a homogeneous effective medium that combines the hydrodynamic effects of both the solvent and the rigid disks. Applying shear rate $\dot{\gamma}$ to such a medium, results in a homogeneous distribution of viscous stress with an average value $\sigma_{xy}^{MF} = \dot{\gamma}\eta_{MF}$, where η_{MF} is the viscosity of the effective medium which we can approximate by the viscosity of a dilute suspension of disks

$$\eta_{MF} = \eta_0(1 + 2\phi + o(\phi)). \tag{C2}$$

Since the forces acting in the disk are proportional to the imposed viscous stress, we get the following expression for the effective viscosity of a semi-dilute suspension in the mean-field approximation η_{MF} :

$$\eta_{MF} = \eta_0[1 + 2\phi(1 + 2\phi) + o(\phi^2)]. \tag{C3}$$

The first correction to expression (C3) takes into account the fact that the disks can not overlap. We calculate this correction in the following way: Given a disk D, we solve for the effective flow created by those disks D_α that overlap with it. The terms of order $o(\phi^2)$ being neglected, this calculation can be performed with the simplification that the effects of all disks D_α can be taken independently from each other and from the disk D. Placing the origin of the coordinate plane at the center of the disk D and denoting the center of the disk D_α as the complex number ζ_α, we observe that disk D_α creates the following distribution of force densities $\Phi(\zeta) = f_x(\zeta) + if_y(\zeta)$:

$$\Phi(\zeta) = 2i\dot{\gamma}\eta \int_0^{2\pi} \delta(\zeta - \zeta_\alpha - ae^{i\sigma})e^{-i\sigma} d\sigma. \tag{C4}$$

The total force density created by disks overlapping with D results from integration of (C4) multiplied by the probability density of finding a disk D_α centered at ζ_α and overlapping with D. This probability density reduces to $\phi H(2a - |\zeta_\alpha|)/(\pi a^2)$ when the disks are independently and homogeneously distributed. Here H is the Heaviside function. Performing the integration, the following density of effective forces is obtained:

$$\Phi^{OL}(\zeta) = 4i\dot{\gamma}\eta\overline{\zeta} \begin{cases} 0 & \text{if } |\zeta| \le a \\ \sqrt{1 - \frac{(3a^2 - |\zeta|^2)^2}{4a^2|\zeta|^2}} & \text{if } a < |\zeta| < 3a \\ 0 & \text{if } |\zeta| \ge 3a, \end{cases} \tag{C5}$$

where $\Phi^{OL} = f_x^{OL} + i f_y^{OL}$ and $\boldsymbol{f}^{OL}$ is the effective force density created by all disks overlapping with the disk D. The flow disturbance produced by the forces (C5) has a complicated form but in the region occupied by the disk D, a simple straining flow is recovered:

$$\xi^{OL}(\zeta) = i\dot{\gamma}\frac{\overline{\zeta}}{2} \quad \text{if } |\zeta| \le a. \tag{C6}$$

Equation (C6) suggests that the disks overlapping with D would create an additional strain rate $\dot{\gamma}\phi^2$ acting inside the disk D, which gives a contribution $2\phi^2\eta_0 + o(\phi^2)$ to the effective viscosity (C3). Subtracting this contribution, we obtain

$$\eta_{NO} = \eta_0[1 + 2\phi(1+\phi)] + o(\phi^2). \tag{C7}$$

for the effective viscosity η_{NO} of suspension of not overlapping not interacting disks. The following intuitive explanation can be given to the expression (C7): The average of the rate of strain $\partial_x u_y + \partial_y u_x$ in a suspension subjected to a shear rate $\dot{\gamma}$ is equal to $\dot{\gamma}$. This average can be decomposed into two contributions: the rate of strain inside the disks is equal to 0 and enters the average rate of strain in the whole suspension with the weight ϕ. The average rate of strain inside the suspending fluid has weight $1-\phi$ and, therefore, must be equal to $\dot{\gamma}/(1-\phi) = \dot{\gamma}[1+\phi+o(\phi)]$ for the average rate of strain in the whole suspension to be equal to $\dot{\gamma}$. This means that each disk D in the suspension is subject to an effective rate of strain equal to $\dot{\gamma}[1+\phi+o(\phi)])$ due to the presence of the other disks if we neglect the effect of the presence of the disk D on the distribution of velocities in the suspension. Because the coefficient A_1 in (C1) is proportional to the rate of strain acting on the disk, we obtain the result (C7).

The second correction must be applied to expression (C7) in order to account for the short range hydrodynamic interactions between the disks. Indeed, expression (C7) was calculated with the simplification that when calculating the hydrodynamic effect of a disk D_1 on a disk D_2, the state of D_1 is taken as if no other disks, including D_2, were not present. This effectively corresponds to neglecting all terms of order $o((a/r)^2)$ in expression (B8). Calculating the contribution of these terms to the effective viscosity of the semi-dilute suspension requires averaging all but the first two terms in the right hand side of expression (B7) over all possible relative positions of the two disks:

$$\eta_{eff} = \eta_{NO} - \frac{4\phi^2}{\pi a^2\dot{\gamma}}\int_0^{2\pi} d\theta \int_{2a}^{\infty} r dr \delta\Im A_1^{PW}(r,\theta), \tag{C8}$$

where $\delta\Im A_1(r,\theta)$ is the correction to the value of $\Im A_1$

$$\delta\Im A_1 = \Im A_1^{PW} - \dot{\gamma}\left(-\frac{a^2}{2} - \frac{a^4\cos 4\theta}{r^2}\right). \tag{C9}$$

The integral (C8) converges absolutely thanks to the fact that the leading terms in (B8) were split off and averaged during the calculation of η_{NO} in (C7). This allows us to perform the integration (C8) for a given number of terms in the expansion (B8). Taking the a^6/r^4 term in (B8) yields $\eta_{eff} \approx \eta_{NO} + 2\eta_0\phi^2 + o(\phi^2) = \eta_0(1 + 2\phi + 4\phi^2)$, which coincides with the result reported in [37], where the same truncation of (B8) was performed. Averaging further terms in (B8) results in a slightly lower value of the Batchelor coefficient β. Truncating the expansion of A_1^{PW} at the term $(a/r)^{64}$ gives us $\beta \approx 3.6$. The result of integration (C8) is plotted as a function of k_{max}, the number of terms taken in the expansion (B8) in figure 16. The convergence is rather slow because of the non-analytical behavior of A_1^{PW} at $r = 2a$, which corresponds to the case when the two disks touch each other.

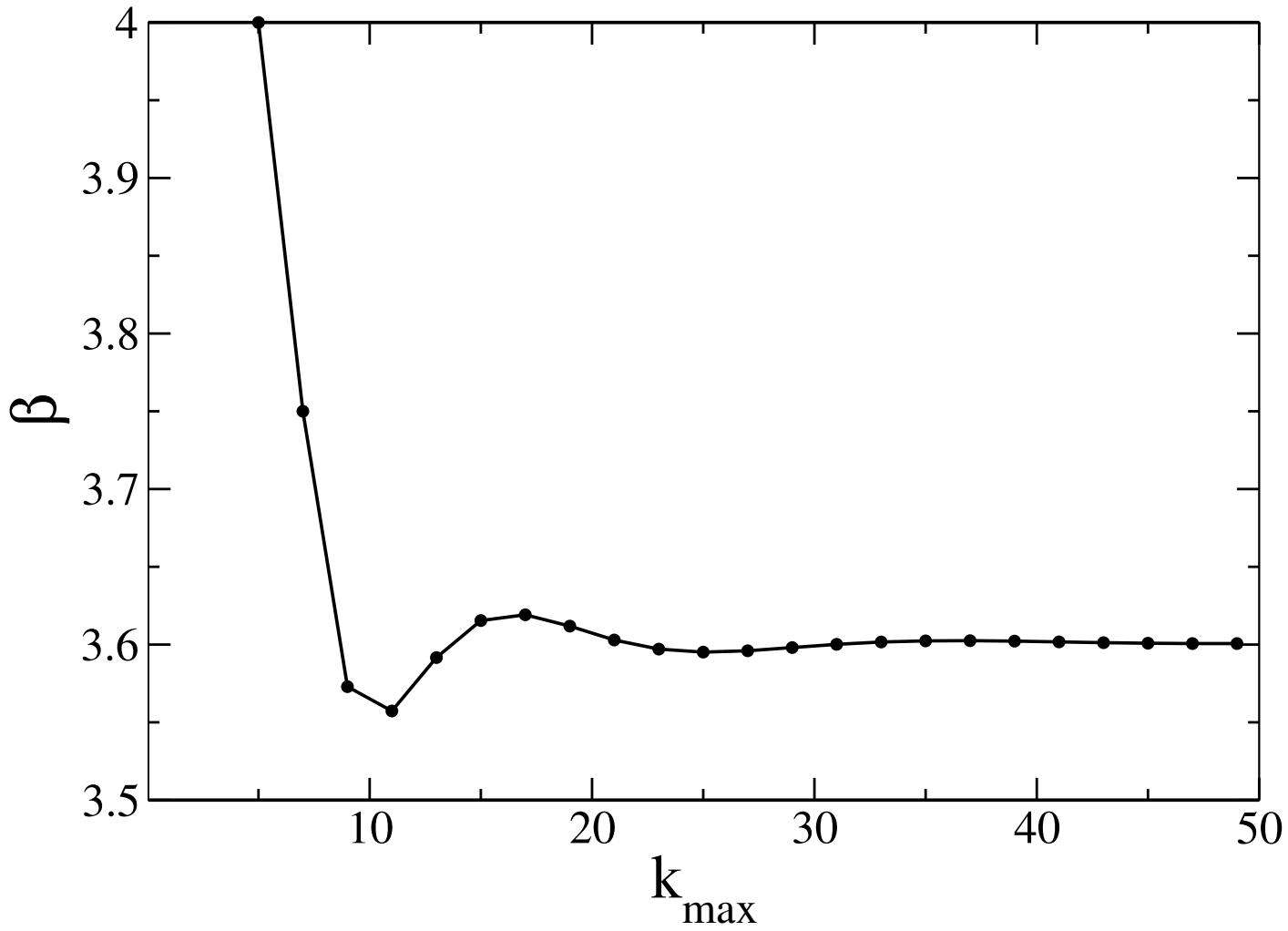

FIG. 16. Analytical result for Batchelor coefficient β of an unconfined suspension of rigid disks, shown as a function of k_{max}, the order of truncation of expansion of $\Im A_1$ in powers of a/r (cf. eq. (B8)). The results are shown only for even values of k_{max} because there are no odd powers in the expansion of $\Im A_1$. For $k_{max} = 4$, $\beta \simeq 4$, for large k_{max} β is close to 3.6.

Appendix D: Disk near a flat wall

The solution of the problem of two interacting disks can be easily modified to solve the problem of a disk near a flat wall. We place the wall at position $\Im\zeta = 0$ of the complex plane and denote the center of the disk as the complex number $\zeta_0 = iah_0$, where ah_0 is the distance of the center of the disk from the wall, as defined above. The velocity field $\xi = u_x + iu_y$ can be written in the following form

$$\begin{aligned}\xi(\zeta) = A(\zeta - \zeta_0) - (\zeta - \overline{\zeta})\overline{A'(\zeta - \zeta_0)} - A(\overline{\zeta} - \zeta_0) + \\ + B(\overline{\zeta} - \overline{\zeta}_0) - B(\zeta - \overline{\zeta}_0) + (\zeta - \overline{\zeta})\overline{B'(\zeta - \overline{\zeta}_0)},\end{aligned} \tag{D1}$$

which automatically satisfies the Stokes equation and the no slip boundary condition at the wall. The ansatz (D1) is a two-dimensional adaptation ([50]) of the the Blake solution ([51]) recast in the complex form. The functions A and B can be represented as Laurent series about point ζ_0, the coefficients of which can be found according to the scheme outlined in Appendix B. The following result is then obtained:

$$[\eta]_{1\,wall} = 2 + \frac{2}{h_0^2} - \frac{1}{4h_0^4} + \frac{15}{16h_0^6} - \frac{49}{128h_0^8} + \\ + \frac{47}{128h_0^{10}} + \frac{35}{512h_0^{12}} + o(1/h_0^{12}). \tag{D2}$$

The convergence of the expansion (D2) is presented in Fig. 17.

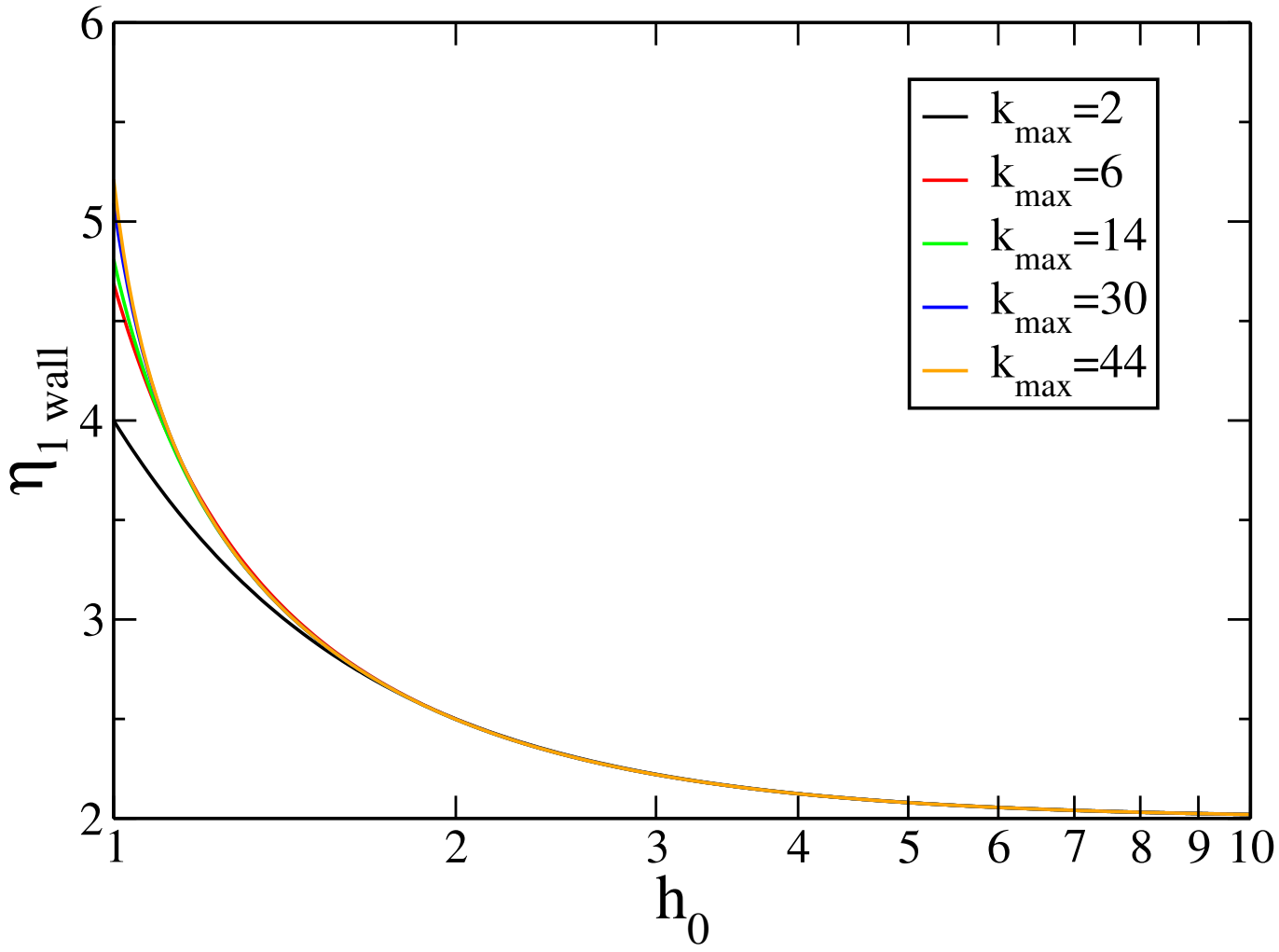

FIG. 17. Convergence of the analytical expression for the intrinsic viscosity contribution $[\eta]_{1\,wall}$ of a disk near a rigid wall, shown as a function of h_0 for several values of k_{max}, the order of truncation of expansion of $[\eta]_{1\,wall}$ in powers of $1/h_0$ (eq. (D2)).

[1] N. Frankel and A. Acrivos, Chem. Eng. Sc. **22**, 847 (1967).
[2] E. Guazzelli and J. Morris, *A physical Introduction to Suspension Dynamics* (Cambridge University Press, 2012).
[3] S. Kim and S. Karilla, *Microhydrodynamics: principles and selected applications* (Butter-worths, 1989).
[4] S. Lee and L. Leal, J. Fluid Mech. **164**, 401 (1986).
[5] C. Robertson and A. Acrivos, J. Fluid Mech. **40**, 685 (1970).
[6] T. Dodd, D. Hammer, A. Sangani, and D. Koch, J. of Fluid Mech. **293**, 147 (1995).
[7] M. Thiebaud, Z. Shen, J. Harting, and C. Misbah, Phys. Rev. Lett. **112**, 238304 (2014).
[8] G. Ghigliotti, T. Biben, and C. Misbah, J. Fluid. Mech. **653** (2012).
[9] P. Rao, G. Zahalak, and S. Sutera, J. Fluid Mech. **270**, 73 (1994).
[10] H. Woolfenden and M. Blyth, J. Fluid Mech. **669**, 3 (2011).
[11] C. K. Aidun and Y. Lu, J. Stat. Phys. **81**, 49 (1995).
[12] J. Kromkamp, D. van den Ende, D. Kandhai, R. van der Sman, and R. Boom, Chem. Eng. Sci. **61**, 858 (2006).
[13] B. Cui, H. Diamant, B. Lin, and S. Rice, Phys. Rev. Lett. **92**, 258301 (2004).
[14] S. Bhattacharya, J. Blawzdziewicz, and E. Wajnryb, Phys. of Fluids **541**, 263 (2005).
[15] S. Bhattacharya, J. Blawzdziewicz, and E. Wajnryb, J. Fluid Mech. **18**, 053301 (2006).
[16] M. Staben, A. Zinchenko, and R. Davis, Phys. Fluids **15**, 1711 (2011).
[17] J. Swan and J. Brady, Phys. Fluids **22**, 103301 (2010).
[18] J. Swan and J. Brady, J. Chem. Phys. **135**, 014701 (2011).
[19] Y. Davit and P. Peyla, Eur. Phys. Lett. **83**, 64001 (2008).
[20] P. Peyla and C. Verdier, Eur. Phys. Lett. **94**, 44001 (2011).
[21] A. Sangani, A. Acrivos, and P. Peyla, Physics of Fluids **23**, 083302 (2011).
[22] M. Brust, O. Aouane, M. Thiebaud, D. Flormann, C. Verdier, L. Kaestner, M. Laschke, H. Selmi, A. Benyoussef, T. Podgorski, G. Coupier, C. Misbah, and C. Wagner, Scientific Report **4**, 4348 (2014).
[23] M. Lyon and L. Leal, J. Fluid Mech. **363**, 25 (1998).
[24] P. Nott and J. Brady, J. Fluid Mech. **275**, 157 (1994).
[25] H. Ez-Zahraouy, H. Mansouri, A. Benyoussef, P. Peyla, and C. Misbah, EPL **79** (2007), 10.1029/0295-5075/79/54002.
[26] Y. Davit, J. M. Osborne, H. M. Byrne, D. Gavaghan, and J. Pitt-Francis, Phys. Rev. E **87**, 042724 (2013).
[27] P. Tabeling, *Introduction to microfluidics* (Oxford University Press, 2005).
[28] W. Fornari, L. Brandt, P. Chaudhuri, C. Lopez, D. Mitra, and F. Picano, Phys. Rev. Lett **116**, 018301 (2016).
[29] I. M. Krieger and T. J. Dougherty, Trans. Soc. Rheol. **3**, 137 (1959).
[30] A. Einstein, Ann. Phys. **19**, 289 (1906).
[31] A. Einstein, Ann. Phys. **34**, 591 (1911).
[32] G. K. Batchelor and J. T. Green, J. Fluid. Mech. **56**, 401 (1972).
[33] B. Cichocki and B. U. Felderhof, J. Chem. Phys. **89**, 1049 (1988).
[34] H. S. Chen and A. Acrivos, Int. J. Solids Struct. **14**, 331 (1978).
[35] M. Belzons, R. Blanc, J.-L. Bouillot, and C. Camion, C. R. Acad. Sci. Paris **5**, 292 (1981).
[36] J. Brady, Int. J. Multiphase Flow **10**, 113 (1984).
[37] J. W. Ju and X. D. Zhang, Int. J. Solids Structures **35** (1998).
[38] J. Janela, A. Lefebvre, and B. Maury, in *ESAIM: Proc*, Vol. 14 (2005) pp. 115–123.
[39] A. Lefebvre, in *ESAIM: Proc*, Vol. 18 (2007) pp. 120–132.
[40] H. Tanaka and T. Araki, Phys. Rev. Lett. **85**, 1338 (2000).
[41] P. Peyla, EPL **80**, 34001 (2007).
[42] B. Maury, SIAM Journal on Numerical Analysis **47**, 1126 (2009).
[43] L. Jibuti, S. Rafaï, and P. Peyla, J. of Fluid Mech. **693**, 345 (2012).
[44] V. Girault and P. Raviart, *Finite element methods for Navier-Stokes equations: theory and algorithms* (Springer Verlag, 1986).
[45] V. Doyeux, T. Podgorski, S. Peponas, M. Ismail, and G. Coupier, Journal of Fluid Mechanics **674**, 359 (2011).
[46] F. Hecht, J. Numer. Math. **20**, 251 (2012).
[47] J. Happel and H. Brenner, *Low Reynolds number hydrodynamics* (Martinus Nijhoff Publishers, The Hague, 1983).
[48] A. Shapere and F. Wilczek, Phys. Rev. Lett. **58**, 2051 (1987).
[49] G. K. Batchelor, J. Fluid. Mech. **41**, 545 (1970).
[50] C. Pozrikidis, *Boundary Integral and Singularity Methods for Linearized Viscous Flow* (Cambridge University Press, 1992).
[51] J. Blake, J. Fluid Mech. **46**, 199 (1971).